

## **Reply to Referee #1**

### **General comments:**

*The impact of external thermal forcing induced atmospheric circulation changes on air quality is an important issue in atmospheric environment study. Focusing this scientific issue, this manuscript presented an interesting finding on two pathways of thermal forcing sources in the North Atlantic region (R1) and the western North Pacific region (R2) drive the interannual variations of autumnal haze pollution in the air pollution region of North China via the tele-connection analysis and AGCM simulation, which could improve our understanding and prediction on air quality change in China, Asia and the Northern Hemisphere. This manuscript falls within the scope of ACP. I suggest the minor revisions before it is published as follows:*

**Reply:** Thank you for your positive comments. We have revised the manuscript based on your comments/suggestions. Below is our point-by-point reply to these comments/suggestions (italic is for original comments and non-italic is our replies).

### **Specific comments:**

**1)***Please add the discussions on the tele-connection pattern from the R1 region to North China in connection with North Atlantic Oscillation, and the R2 region in association with Western Pacific Warm Pool.*

**Reply:** Thanks for your comment. We have added two relevant references and corresponding discussions. Please see **Lines 220-223** and **Lines 254-255** in the revised manuscript for the discussions.

(Lines 220-223) “Intriguingly, from the surface projection of the above quasi-barotropic teleconnection pattern, we can discern a positive phase of North Atlantic Oscillation-like mode in connection with this pattern (Hurrell and Deser, 2009).”

(Lines 254-255) “...with its southern portion belonging to the Western Pacific Warm Pool (You et al., 2018).”

### **Reference:**

Hurrell, J. W., and Deser, C.: North Atlantic climate variability: The role of the North Atlantic Oscillation, *J Marine Syst*, 78, 28-41, 10.1016/j.jmarsys.2008.11.026, 2009.

You, Y. C., Cheng, X. G., Zhao, T. L., Xu, X. D., Gong, S. L., Zhang, X. Y., Zheng, Y., Che, H. Z., Yu, C., Chang, J. C., Ma, G. X., and Wu, M.: Variations of haze pollution in China modulated by thermal forcing of the Western Pacific Warm Pool, *Atmosphere*, 9, 314, 10.3390/atmos9080314, 2018.

2) Please modify the lines 20-21: the joint impacts can greatly enhance the likelihood of a higher  $AHD_{BTH}$ . Observational and simulation evidence suggests that SST anomalies can affect the variation....

**Reply:** Thanks for your comment. The modification was done. Please see Lines 22-24 in the revised manuscript.

Lines 22-24: "...When the autumnal SST warming in R1 and R2 are both significant, the likelihood of a higher  $AHD_{BTH}$  is greatly enhanced. Observational and simulation evidence demonstrated how SST anomalies over R1 and R2 influence variation of  $AHD_{BTH}$  via two different pathways."

3) Lines 191 and 193, please add "surface air" before "temperature".

**Reply:** Thanks for your suggestion. We have added "surface air" before "temperature". Please see Line 205 in the revised manuscript.

Line 205: "...and surface air temperature (Fig. 4b), ..."

4) Please add the box outlines the research domain of the BTH region in Fig. 7.

**Reply:** Thanks for your constructive suggestion. We have added the blue dashed box outlining the research domain of the BTH region. Please see Fig. 7 in the revised manuscript.

### **Reply to Referee #2**

#### **General comments:**

*This paper provides a new possible signal source in the North Atlantic subtropical sector (R1) and the western North Pacific sector (R2) for autumnal haze days (AHD) in the Beijing-Tianjin-Hebei region (BTH region) via the tele-connection mode. The effect sequence of the warm phase of these two oceanic sources on the AHD in BTH is basically reasonable, leading to depressed planetary boundary layer and subsidence of the atmosphere. These changing meteorological conditions are the favorable background for the higher AHD in BTH. The methodology used in this paper is correct (i.e. Rossby wave train). The findings obtained by this paper may be useful to make the seasonal outlook of the air pollution condition in autumn.*

**Reply:** Thank you for your positive comments. We have revised the manuscript based on your comments/suggestions. Below is our point-by-point reply to these comments/suggestions (italic is for original comments and non-italic is our replies).

**Specified corrections:**

*(1) For the SST of the North Atlantic, why only the middle oceanic region is selected? The representative signal source of the AMO should be the triple-pole SST pattern, with high-latitude and the tropical poles being more important.*

**Reply:** Thanks for your comment. The AMO is known as the SST in the North Atlantic varying on the basin scale and at period of around 65–80 years. Since our study concentrated on the interannual variability, the AMO is not relevant to our research target.

We chose subtropical North Atlantic region (22°–32°N, 90°–40°W) as the key SSTA region for the following two reasons. Firstly, the subtropical North Atlantic SSTA is the only region over North Atlantic that highly correlated with the  $AHD_{BTH}$  on interannual timescale. Although the regression SSTA pattern over North Atlantic looks like a tri-pole SST pattern (NAT SST pattern for short) which has profound impacts on Eurasian climate, the relationship between  $AHD_{BTH}$  and simultaneous NAT SST pattern is insignificant. The correlation coefficient between  $AHD_{BTH}$  and NAT SST triple-pole index (Deser and Michael, 1997) is only 0.17. Therefore, we chose the middle oceanic region of North Atlantic as the key region for  $AHD_{BTH}$ .

Secondly, the positive correlated SSTA over that region can induce positive rainfall anomaly (diabatic heating). Therefore, the SSTA should play an active role in local air-sea interaction and in turn influence the large-scale circulation through inducing teleconnection.

To sum up, we chose subtropical North Atlantic region (22°–32°N, 90°–40°W) as the key driving region from both statistical diagnosis and physical basis.

We have added this discussion in the revised manuscript (Lines 256-265).

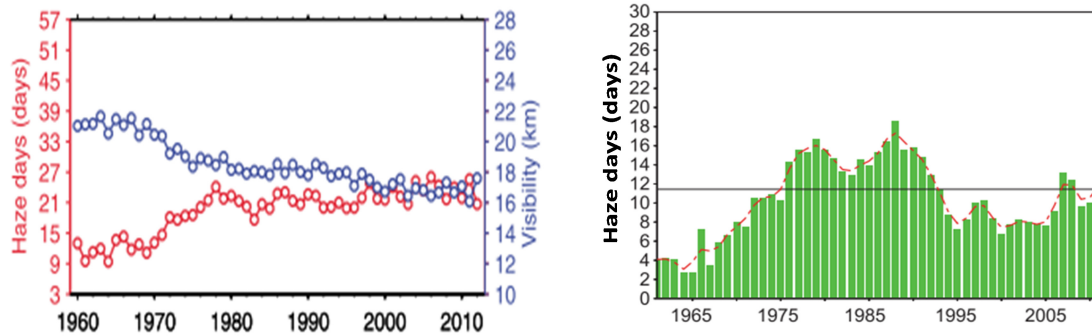
**Reference:**

Deser, C. and Michael S.T., 1997: Atmosphere-ocean interaction on weekly timescales in the North Atlantic and Pacific. *Journal of Climate*, 10(3): 393-408.

*(2) From Figure 2, one can see the rapid increase of AHD in BTH. However, other studies have shown that the rapid increase in AHD started from the mid-ninety of 20 century or early in this century. Please compare the difference between them and explain why.*

**Reply:** Thanks for your constructive comments. After checking many related literatures (e.g., **Figure 6b** in Fu and Dan, 2014), we found that the annual total haze days indeed showed the rapid increase in the BTH region since the early 21st century, but it is not materialized for the case of autumn season.

For the autumn season, from the previous studies, we found that the rapid increase in AHD over North China did not start from the mid-ninety of 20 century or early in this century (**R-Figure 1**). Our results are quite consistent with the previous studies.



**R-Figure 1.** Time series of AHD in North China. (left) Adapted from *Chen and Wang (2015)*. (right) Adapted from *Ding and Liu (2014)*. The red dashed line is 9-point smooth curve.

**Reference:**

Chen, H. P., and Wang, H. J.: Haze Days in North China and the associated atmospheric circulations based on daily visibility data from 1960 to 2012, *J Geophys Res Atmos*, 120, 5895-5909, 10.1002/2015JD023225, 2015.

Ding, Y. H., and Liu, Y. J.: Analysis of long-term variations of fog and haze in China in recent 50 years and their relations with atmospheric humidity, *Sci China Earth Sci*, 57, 36-46, 10.1007/s11430-013-4792-1, 2014.

Fu, C. B., and Dan, L.: Spatiotemporal characteristics of haze days under heavy pollution over central and eastern China during 1960–2010, *Climatic and Environmental Research (in Chinese)*, 19 (2), 219-226, 2014.

**(3)** For Figure 6, please indicate the significance level for the correlation coefficient.

**Reply:** Thanks for your suggestion. We have added the significance level for the correlation coefficient as suggested. Please see Figure 6 in the revised manuscript.

**(4)** The anticyclonic circulation over Northeast China-Okhotsk Sea at 850 hPa is a critical system. Please check if it only takes place in autumn (or/and winter)? Whether or not it already exists in summer?

**Reply:** Thanks for your good comment and suggestion. As you indicated, the 850-hPa anomalous anticyclonic circulation over Northeast China-Okhotsk Sea is indeed a critical system that having significant impacts upon the interannual variability of AHD<sub>BTH</sub>. In addition to autumn season, this system also takes place in winter (e.g., **Figure 4b** in Yin et al., 2017; **Figure 3a** in Zhong et al., 2018), which greatly influences the interannual changes of wintertime haze pollution.

However, this anticyclonic circulation does not exist in the prior summer based on our correlation analysis (figures omitted). Therefore, we could infer that this

anticyclonic circulation anomaly over Northeast Asia is only occurred in the simultaneous autumn and winter.

**Reference:**

Yin, Z. C., Wang, H. J., and Chen, H. P.: Understanding severe winter haze events in the North China Plain in 2014: roles of climate anomalies, *AtmosChemPhys*, 17, 1641-1651, 10.5194/acp-17-1641-2017, 2017.

Zhong, W. G., Yin, Z. C., Wang, H. J., and: The Relationship between the Anticyclonic Anomalies in Northeast Asia and Severe Haze in the Beijing–Tianjin–Hebei Region, *AtmosChem Phys, Discuss.*, 10.5194/acp-2018-782, in review, 2018.

*(5) From Figure 10(a), the descending motion seems to be out of BTH region. Please explain it.*

**Reply:** Thanks for your comment. Except for a small portion of upward motion over the southern BTH region, most of the BTH region is indeed dominated by air subsidence from mid-to-upper troposphere (700-300 hPa in Figure 10a).

The significant descending motion is tied to strong ascending motion over south of the BTH region. Because the ascending motion is so strong, it makes the descending motion farther to the north. Nevertheless, this subsidence could enhance Northeast Asian anticyclonic anomaly.

*(6) The warm R2 should be associated with the El Nino event. Therefore, according the EAP pattern, it could be “- + -“ meridional circulation pattern. Please attention to this point and further properly modify the position A in Figure 13.*

**Reply:** Thanks for your insightful suggestion. The El Niño event related to EAP pattern (or PJ pattern) mainly appears in boreal summer. The present study focuses on the autumn season. We think Northeast Asian anticyclonic anomaly is not part of the EAP pattern, but rather a joint result of the mid-latitude Rossby wave train emanating from Atlantic to East Asia, and an anomalous local meridional circulation forced by western North Pacific SSTA.

# Two pathways of how remote SST anomalies drive the interannual variability of autumnal haze days in the Beijing–Tianjin–Hebei region, China

Jing Wang<sup>1</sup>, Zhiwei Zhu<sup>1\*</sup>, Li Qi<sup>1</sup>, Qiaohua Zhao<sup>1</sup>, Jinhai He<sup>1</sup>, and Julian X. L. Wang<sup>2</sup>

<sup>1</sup>Key Laboratory of Meteorological Disaster, Ministry of Education (KLME)/Joint International Research Laboratory of Climate and Environment Change (ILCEC)/Collaborative Innovation Center on Forecast and Evaluation of Meteorological Disasters (CIC-FEMD), Nanjing University of Information Science and Technology, Nanjing, China

<sup>2</sup>Air Resources Laboratory, National Oceanic and Atmospheric Administration, College Park, MD, USA

\* Correspondence to: Zhiwei Zhu (zww@nuist.edu.cn)

**Abstract.** Analogous to the circumstances in wintertime, the increasing severity of autumnal haze pollution over the Beijing–Tianjin–Hebei (BTH) region may also lead to impairment of the socioeconomic development and human health in this region. Despite manmade aerosol emissions, the interannual variability of autumnal (September–October–November) haze days (AHD) in the BTH region ( $AHD_{BTH}$ ) is apparently tied to the global and regional meteorological anomalies. The present study suggests that an above-normal  $AHD_{BTH}$  is closely associated with the simultaneous sea surface temperature (SST) warming in two regions [over the North Atlantic subtropical sector (R1) and over the western North Pacific sector (R2)]. ~~When the autumnal SST warming in R1 and R2 are both remarkably significant, the joint impacts can greatly enhance the likelihood of a higher  $AHD_{BTH}$ . Observational and simulation evidence suggests that SST anomalies can affect the variation in  $AHD_{BTH}$  via two different pathways.~~ When the autumnal SST warming in R1 and R2 are both significant, the likelihood of a higher  $AHD_{BTH}$  is greatly enhanced. Observational and simulation evidence demonstrated how remote SST anomalies over R1 and R2 influence variation of  $AHD_{BTH}$  via two different pathways. Firstly, SST warming in R1 can induce a downstream mid-latitude Rossby wave train, leading to a barotropic high-pressure and subsidence anomaly over the BTH region. Secondly, SST warming in R2 can also result in air subsidence over the BTH region through an anomalous local meridional cell. Through these two distinct pathways, localized meteorological circumstances conducive to a higher  $AHD_{BTH}$  (i.e., repressed planetary boundary layer, weak southerly airflow, and warm and moist conditions) can be established.

## 1 Introduction

Aerosol particles (APs) are ubiquitous in the ambient air. Through aerosol-induced thermal forcing, APs can exert profound impacts on regional and large-scale circulation (e.g., Chung et al., 2002; Lau and Kim, 2006; Lau et al., 2006; Liu et al., 2009; Li et al., 2016; Wu et al., 2016), as well as global warming (e.g., Charlson et al., 1992; Tett et al., 1999; Zhang et al., 2016). Notably, due to the property of light extinction related to high concentrations of APs, especially fine particulate matter [i.e., particulate matter (PM) with an aerodynamic diameter of 2.5  $\mu\text{m}$  or less ( $PM_{2.5}$ )] (Guo et al., 2014; Wang et al., 2014; Li et al., 2017; Seo et al., 2017; Chen et al., 2018; Luan et al., 2018), severe haze weather with low visibility ~~and high concentrations of gas pollutants~~ can readily occur (Chen et al., 2012; Li et al., 2016; Ding et al., 2017; Seo et al., 2017; Chen et al., 2018).

In recent decades, observational evidence suggests that China has become one of the most severe AP-loading regions in the world (Tao et al., 2016; Li et al., 2016), arguably because of the country's nationwide rapid industrialization and urbanization (Xu et al., 2015; Zhang et al., 2016). High concentrations of APs can lead to the formation of severe haze weather via complicated interactions (Wang et al., 2014). Haze weather is not only harmful to the human respiratory and cardiovascular systems (Pope III and Dockery, 2006; Tie et al., 2009; Chen et al., 2013; Xu et al., 2013), but also influences vehicular traffic and crop yields (Chameides et al., 1999; Wu et al.,

50 | 2005). As a result, haze pollution has received considerable attention from ~~both~~ the government  
51 | and the public. Unfortunately, on the one hand, overwhelming industrialization leads to more  
52 | severe haze contamination over the Beijing–Tianjin–Hebei (BTH) region (Yin ~~et al.~~ and Wang,  
53 | 2016~~5~~); whilst on the other hand, the trumpet-shaped topography (Fig. 1) of the region is  
54 | unfavorable for the dissipation of air pollution, thus making the BTH region home to some of the  
55 | worst haze weather in China. Since the BTH region is the most economically developed region in  
56 | North China and is at the heart of Chinese politics and culture ~~(not least because it is home to the~~  
57 | ~~capital city, Beijing, and Xiongan New Area, for instance)~~, severe haze pollution in this region has  
58 | become a critical issue (e.g., Mu and Zhang, 2014; Yin ~~et al.~~, 2015; Wang, 2018), especially since  
59 | the occurrence of the unprecedented severe haze event in North China in January 2013 (Wang et  
60 | al., 2014; Zhang et al., 2014; Mu and Zhang, 2014; Tao et al., 2014; Zhang et al., 2015).

61 | To date, numerous efforts have been made to explore the causes of wintertime haze pollution over  
62 | the BTH region and its surroundings, and these ~~efforts~~ previous studies roughly fall into three  
63 | categories ~~of results from~~ based on the climatological perspective. The first category ~~features~~  
64 | ~~studies that have~~ reported that the joint effects of the emissions of various sources of APs (e.g.,  
65 | Cao et al., 2007; Guo et al., 2011; Zhu et al., 2016) and climate anomalies (e.g., Chen and Wang,  
66 | 2015; Wang and Chen, 2016; Yin and Wang, 2016a; Cai et al., 2017; Yin ~~et al.~~, 2017; Yin and  
67 | Wang, 2018; Wang, 2018) may have brought about the increasing severity of haze pollution over  
68 | China in recent decades. The second category of studies, meanwhile, underlines the causality of  
69 | the variation in winter haze days in eastern and northern China from the perspective of climate  
70 | anomalies (e.g., Li et al., 2016; Yin and Wang, 2016b; Yin and Wang, 2018; Pei et al., 2018). For  
71 | instance, it is suggested that a weakened East Asian winter monsoon (EAWM) system ~~has been~~  
72 | ~~suggested as being responsible for~~ could lead to the above-normal numbers of winter haze days  
73 | (e.g., Niu et al., 2010; Li et al., 2016; Yin and Wang, 2016a; Yin and Wang, 2017; Yin ~~et al.~~,  
74 | 2017); ~~—plus~~ Meanwhile, the variability of EAWM's ~~variability~~ has been shown to be  
75 | significantly tied to the East Atlantic–West Russia pattern ~~(Yin et al., 2017; Yin and Wang, 2017)~~  
76 | and Eurasian pattern (Zhang et al., 2016; Yin et al., 2017). The third category ~~of studies~~ focuses on  
77 | the external forcings associated with the variability of winter haze days. These forcings include the  
78 | sea surface temperature (SST) (e.g., Gao and Li, 2015; Wang et al., 2015; Yin and Wang, 2016a;  
79 | Yin ~~et al.~~, 2017), Arctic sea ice (e.g., Wang et al., 2015; Zou et al., 2017), Eurasian snowpack (e.g.,  
80 | Yin and Wang, ~~et al.~~, 2017; Yin and Wang, 2018), and the thermal conditions on the Tibetan  
81 | Plateau (e.g., Xu et al., 2016). However, most of these previous works have focused on wintertime,  
82 | with little attention having been paid to other seasons.

83 | Autumn is a transitional season from the wet and hot ~~conditions of~~ summer to the dry and cold  
84 | ~~conditions of~~ winter. Climatologically, ~~T~~ the weather in autumn over the BTH region is  
85 | ~~climatologically~~ quite pleasant, with favorable temperatures and light winds. Outdoor activities  
86 | and tourism are therefore prevailing important, ~~economically,~~ in the autumn season. However,  
87 | ~~notably,~~ autumn is also a season in which haze weather frequently occurs in the BTH region  
88 | (Chen and Wang, 2015), ~~—).~~ ~~and~~ ~~†~~ The number of autumnal haze days (AHDs) has increased  
89 | remarkably in recent years. Such an increase in the number of haze days is a potential threat to ~~the~~  
90 | ~~outdoor activities and~~ tourism economics in this region ~~that, as mentioned, are so important to the~~  
91 | ~~region at this time of year~~. Therefore, research into the causes of the interannual variation in  
92 | AHDs in the BTH region (AHD<sub>BTH</sub>) is imperative. Such work not only provides scientific support  
93 | to the year-to-year scheduling of anthropogenic emissions for dealing with autumnal haze  
94 | pollution, but also helps the government with facilitating the arrangement of tourism  
95 | ~~economic~~ tourism and outdoor activities. However, ~~as already mentioned,~~ compared to the myriad  
96 | publications studies on wintertime haze pollution, autumn haze pollution over the BTH region has  
97 | attracted far less attention, with only a few case studies on atmospheric circulation having been

98 reported (Yang et al., 2015; Gao and Chen, 2017; Wang et al., 2018). It was this knowledge gap  
99 that motivated us to revisit the variability of  $AHD_{BTH}$ . Considering that the SST acts as a crucial  
100 driver of large-scale climate variability (e.g., Wang et al., 2009; Zhu et al., 2014; He and Zhu,  
101 2015; Xiao et al., 2015; Zhu and Li, 2017; Zhu, 2018), we aimed to figure out the underlying air-  
102 sea interaction mechanisms for the interannual  $AHD_{BTH}$  variability in the present study.

103 The remainder of this paper is organized as follows. Section 2 introduces the data, model and  
104 methodology. Section 3 presents the atmospheric anomalies associated with  $AHD_{BTH}$ . Section 4  
105 addresses the mechanisms ~~and pathways of~~ how remote SST anomalies (SSTAs) ~~in driving~~ the  
106 interannual variations of  $AHD_{BTH}$ . Conclusions and further discussion are provided in the final  
107 section.

108

## 109 **2 Data, model and methodology**

110

### 111 **2.1 Data**

112 The data used in this study are as follows: (1) monthly mean planetary boundary layer height  
113 (PBLH), with a  $1^\circ \times 1^\circ$  horizontal resolution, from the European Centre for Medium-Range  
114 Weather Forecasts Interim Reanalysis (ERA-Interim) (Dee et al., 2011); (2) monthly mean  
115 atmospheric data, with a  $2.5^\circ \times 2.5^\circ$  horizontal resolution, ~~from the National Centers for~~  
116 ~~Environmental Prediction (NCEP) National Center for Atmospheric Research (NCAR)~~  
117 ~~Reanalysis I (NCEP/NCAR) (Kalnay et al., 1996);~~ and total cloud cover (entire atmosphere  
118 considered as a single layer;  $192 \times 94$  points in the horizontal direction), ~~also from NCEP/NCAR~~  
119 ~~from the National Centers for Environmental Prediction (NCEP)–National Center for Atmospheric~~  
120 ~~Research (NCAR) Reanalysis I (NCEP/NCAR) (Kalnay et al., 1996);~~ (3) monthly mean SST, with  
121 a  $2^\circ \times 2^\circ$  horizontal resolution, of the Extended Reconstructed SST dataset, version 5 (ERSST.v5;  
122 Huang et al., 2017), from the National Oceanic and Atmospheric Administration (NOAA); (4)  
123 global monthly precipitation data, with a  $2.5^\circ \times 2.5^\circ$  horizontal resolution, from NOAA's  
124 precipitation reconstruction (Chen et al., 2002); (5) ground-timing observation datasets, at 02:00,  
125 08:00, 14:00 and 20:00 BLT (Beijing local time), from the National Meteorological Information  
126 Center of China. The temporal coverage of the PBLH data is from 1979 to 2017, while the  
127 remaining datasets are from 1960 to 2017. Here, boreal autumn refers to the seasonal mean for  
128 September–October–November (SON).

129

### 130 **2.2 Model**

131 The numerical model ~~used here we employed~~ is an anomaly atmospheric general circulation  
132 model (AGCM) based on the Geophysical Fluid Dynamics Laboratory (GFDL) global spectrum  
133 dry AGCM (Held and Suarez, 1994), ~~which is employed to investigate the mechanisms for the~~  
134 ~~atmospheric responses to the specified SST-induced heating.~~ The horizontal resolution is T42,  
135 with five evenly spaced sigma levels ( $\sigma = p/ps$ ; interval: 0.2; top level:  $\sigma = 0$ ; bottom level:  $\sigma = 1$ ).  
136 A realistic autumn mean state, obtained from the long-term mean of the NCEP/NCAR reanalysis  
137 data, is prescribed as the model basic state. This model has been used to unravel the eddy-mean  
138 interaction over East Asia and its downstream climate impacts ~~on over~~ North America ~~n climate~~  
139 (Zhu and Li, 2016, 2018).

140

141

142



### 143 2.3 Methodology

144 The definition of a haze day in the present study is identical to ~~that used in the~~ previous studies  
145 (~~e.g.~~, Chen and Wang, 2015; ~~Yin et al., 2017; Pei et al., 2018~~). It is based on the ground-timing  
146 observations of relative humidity, visibility and wind speed. It is important to point out that the  
147 visibility observations switched from manual to automatic in 2014, and the visibility threshold for  
148 haze was thus also slightly modified from then on. ~~Nevertheless~~~~However~~, the continuity of the  
149 data was not affected. Following Zhang et al. (2016), the mean number of haze days ( $\overline{\text{NHD}}$ ) for  
150  $\text{AHD}_{\text{BTH}}$  was computed by:

$$151 \quad \overline{\text{NHD}} = \frac{1}{n} \sum_{i=1}^n N \quad (1)$$

152 where  $n$  (here,  $n = 20$ ) is the number of meteorological sites distributed within the BTH region  
153 (Fig. 1), and  $N$  denotes the number of haze days at a site for each autumn.

154 Similar to the approach proposed by Zhu and Li (2017), the 9-yr running mean of the  $\text{AHD}_{\text{BTH}}$   
155 was used to represent the interdecadal component of the  $\text{AHD}_{\text{BTH}}$ , whereas the interannual  
156 component was obtained by removing the interdecadal component from the raw  $\text{AHD}_{\text{BTH}}$ . Since  
157 there is a tapering problem when calculating the running mean, the first four years and the last  
158 four years of the interdecadal component of the  $\text{AHD}_{\text{BTH}}$  could be estimated by the mean value of  
159 the available data with a shorter window. For example, the interdecadal component of the  $\text{AHD}_{\text{BTH}}$   
160 for 2016 and 2017 could be obtained by the mean of 2012–17 and 2013–17, respectively. Note  
161 that the temporal correlation coefficients (TCCs) between the  $\text{AHD}_{\text{BTH}}$  and every single  
162 ~~stationsite~~ were all positive and significant (Fig. 1), indicating ~~the~~ coherency ~~in of~~ the interannual  
163 variability of ~~autumnal~~ haze days ~~in each station~~ over the BTH region; ~~plus~~~~meanwhile~~,  
164 the distribution of these ~~sites~~~~stations~~ was ~~also~~ fairly even. Therefore, the interannual component of  
165 the  $\text{AHD}_{\text{BTH}}$  could be ~~used as a~~ good representation of the year-to-year pollution state over the  
166 whole BTH region in autumn.

167 Linear regression, composite analysis and correlation were used to examine the ~~associated~~  
168 circulation and SST ~~As anomalies that associated with the interannual~~  $\text{AHD}_{\text{BTH}}$ . The two-tailed  
169 Student's  $t$ -test was employed to evaluate the statistical significance of these analyses. The wave  
170 activity flux (WAF; Takaya and Nakamura, 2001) was calculated to depict the tendency of Rossby  
171 wave energy propagation.

### 173 3 Atmospheric anomalies associated with the interannual changes of $\text{AHD}_{\text{BTH}}$

174 Figure 2 illustrates the time series of the raw  $\text{AHD}_{\text{BTH}}$ , along with its interdecadal and interannual  
175 components. A prominent feature is that the  $\text{AHD}_{\text{BTH}}$  displays both interannual and interdecadal  
176 variability. On the interdecadal timescale, the  $\text{AHD}_{\text{BTH}}$  was below average during 1960–1975 and  
177 the late-2000s, but above average during 1975–2003, and it increased dramatically after 2009. On  
178 the interannual timescale, the  $\text{AHD}_{\text{BTH}}$  presents large differences year ~~on by~~ year. For example, the  
179  $\text{AHD}_{\text{BTH}}$  was at its lowest in 2012, but peaked in 2014. Since the interannual variability explains  
180 most of the ~~total~~ variances in the  $\text{AHD}_{\text{BTH}}$  variability, in this study we ~~only~~ investigate the  
181 atmospheric anomalies and unravel the underlying physical ~~processes mechanisms and pathways~~  
182 ~~associated that associated~~ with the  $\text{AHD}_{\text{BTH}}$  on the interannual timescale.

183 Close scrutiny of the large-scale and localized dynamic and thermodynamic fields associated with  
184 the  $\text{AHD}_{\text{BTH}}$  ~~should help in could~~ ~~advancing~~ our understanding of the ~~possible~~ underlying

185 mechanisms. In this regard, we firstly examine the climatological mean autumnal 500-hPa  
186 geopotential height (Z500), 850-hPa winds (UV850) and total cloud, along with the surface  
187 relative humidity and surface air temperature that potentially impact the climate over the BTH  
188 region (Fig. 3). There is a shallow mid-tropospheric trough over coastal East Asia (Fig. 3a), which  
189 resembles the trough in winter (Zhao et al., 2018; Pei et al., 2018) but with a smaller magnitude.  
190 Behind the trough, a clear anticyclonic circulation appears over the central-eastern China, with  
191 remarkable westerly/northwesterly winds dominating the BTH region (Fig. 3a). ~~Cold-Cool~~ and dry  
192 air from higher latitudes is advected by the winds, and the BTH region is thus much cooler and  
193 drier and has less cloud than other regions at the same latitudes (e.g., the central ~~portion of~~ Japan).  
194 As such, the autumnal BTH region features breezy and windy conditions ~~climatologically~~, with  
195 low surface relative humidity (Fig. 3b), reducing the likelihood of haze there via the effect of cold  
196 advection ~~and~~ ventilation ~~effect~~. Note, however, that if the breezy conditions are interrupted, haze  
197 pollution ~~may be enhanced~~ is likely to occur. One may ask whether a higher AHD<sub>BTH</sub> is related to  
198 the interference of such breezy conditions. Figures 4 and 5 were therefore plotted to examine the  
199 associated atmospheric parameters/circulations. For simplicity, the regression and composite  
200 analyses in this study reported hereafter are interpreted with respect to positive phase of AHD<sub>BTH</sub>  
201 anomalies only.

202 Previous studies have revealed that haze pollution is closely correlated with local meteorological  
203 parameters in the planetary boundary layer (e.g., You et al., 2017; Chen et al., 2018). Figure 4  
204 suggests that an above-normal AHD<sub>BTH</sub> is tied to a localized ~~increase enhancement~~ of surface  
205 relative humidity (Fig. 4a) and surface air temperature (Fig. 4b), along with suppressed surface  
206 wind speed (Fig. 4c), sea-level pressure (SLP) (Fig. 4d) and PBLH (Fig. 4e). ~~Specifically, it seems~~  
207 ~~that autumnal haze pollution is more significantly correlated with temperature and PBLH. The~~  
208 question is, what causes the above anomalous parameters that are favorable for a higher  
209 AHD<sub>BTH</sub>?

210 Figure 5 shows the associated large-scale atmospheric circulation anomalies at different levels of  
211 troposphere. ~~From In~~ Figs. 5a–5d, the most noticeable feature is that there is a planetary-scale,  
212 quasi-barotropic Rossby wave train emanating from the North Atlantic subtropical sector. In  
213 addition to an anticyclonic anomaly centered over the North Atlantic subtropics, this  
214 teleconnection pattern has another two pairs of anomalous cyclones (low pressure) and  
215 anticyclones (high pressure) stretching across Eurasia to the ~~North Pacific~~ Northeast Asia, i.e., a  
216 cyclonic anomaly centered over the ocean south of Greenland, an anticyclonic anomaly centered  
217 over Scandinavia, a cyclonic anomaly centered over the adjacent central Siberia, and an Northeast  
218 Asian anticyclonic anomaly centered over the Sea of Japan (SJ). In general, based on the regressed  
219 atmospheric fields, the teleconnection has a much larger amplitude in the upper troposphere (Fig.  
220 5a), ~~rather than that~~ in the mid-troposphere (Fig. 5b) and lower troposphere (Fig. 5c). Intriguingly,  
221 from the surface projection of the above quasi-barotropic teleconnection pattern, we can discern a  
222 positive phase of North Atlantic Oscillation -like mode in connection with this pattern (Hurrell and  
223 Deser, 2009).

224 Among all the height anomalies within the teleconnection, the anomalous quasi-barotropic  
225 Northeast Asian anticyclonic anomaly centered over the SJ ( $A_{SJ}$ ) plays a direct role in driving a  
226 higher AHD<sub>BTH</sub>. The related ~~physical~~ physico-meteorological causes are as follows: There are  
227 southerly/southeasterly anomalies along the western flank of the  $A_{SJ}$  in the lower troposphere (Figs.  
228 5c and 5d), manifesting the capability of suppressed atmospheric horizontal diffusion and thus  
229 favoring a buildup of substantial local and nonlocal APs and warmer moisture over the BTH  
230 region (Yang et al., 2015; Yang et al., 2016) under the specific topographical forcing of the  
231 Taihang Mountains and Yan Mountains (Fig. 1). On the other hand, the significant positive

232 pressure anomaly in the mid-to-upper parts of the  $A_{SJ}$  (Figs. 5a and 5b) not only impedes the  
233 intrusion of cold air into the BTH region, but also facilitates consistent air subsidence over the  
234 BTH region and its surrounding areas (Fig. 4f), resulting in the decrease of the PBLH and  
235 ~~increase~~ amplification of static stability (i.e., the dampened vertical dispersion of the atmosphere).  
236 Consequently, the meteorological conditions connected to a higher  $AHD_{BTH}$  are ~~adverse to quite~~  
237 ~~different from~~ the autumn climate mean state climatological characteristics (Fig. 3).

238 To summarize, the  $A_{SJ}$  and the associated subsidence can induce the capacity for suppressed local  
239 horizontal and vertical dispersion over the BTH region and its surrounding areas, as shown in the  
240 above-mentioned anomalous parameters ~~in the boundary layer~~ (Fig. 4); and these parameters are  
241 further responsible for the accumulation and secondary formation/hygroscopic growth of APs  
242 (Jacob and Winner, 2009; Ding and Liu, 2014; Mu and Liao, 2014; Jia et al., 2015). As such, the  
243 haze pollution over the BTH region is readily established within a narrow space. ~~Therefore, The~~  
244 ~~the~~ question of how the above-normal  $AHD_{BTH}$  is stimulated could plausibly be transferred into  
245 ~~questioning the pathways of~~ how the  $A_{SJ}$  is developed and sustained. In fact, the  $A_{SJ}$  and the  
246 associated air subsidence are modulated by remote SSTAs. We tackle the underlying  
247 mechanisms ~~this issue~~ in the next section.

248

## 249 ~~4 Possible m~~ Mechanisms of the $A_{SJ}$ and pathways

250

### 251 4.1 Observational diagnoses

252 Figure 5c shows that an above-normal  $AHD_{BTH}$  is closely correlated with SST warming in two key  
253 regions: One is the North Atlantic subtropical sector (R1: 22°–32°N, 90°–40°W), and the other is  
254 the western North Pacific sector (R2: 10°–30°N, 108°–140°E), with its southern portion belonging  
255 to the Western Pacific Warm Pool (You et al., 2018). One may ask why we chose these two key  
256 SSTA regions. Firstly, the subtropical North Atlantic SSTA is the only region over North Atlantic  
257 that highly correlated with the  $AHD_{BTH}$  on interannual timescale. Although the regression SSTA  
258 pattern over North Atlantic looks like a tri-pole SST pattern which has profound impacts on  
259 Eurasian climate, the relationship between  $AHD_{BTH}$  and simultaneous NAT SST pattern is  
260 insignificant. The correlation coefficient between  $AHD_{BTH}$  and NAT SST triple-pole index (Deser  
261 and Michael, 1997) is only 0.17. Therefore, we chose the middle oceanic region of North Atlantic  
262 as the key region for  $AHD_{BTH}$ . Secondly, the positive correlated SSTA over R1 and R2 region can  
263 both induce positive rainfall anomaly (diabatic heating), the SSTA should play an active role in  
264 local air-sea interaction and in turn influence the large-scale circulation. Therefore, we chose the  
265 R1 and R2 as the key SSTA regions from both statistical diagnosis and physical basis. Meanwhile,  
266 from Fig. 5e we can discern that enhanced and significant precipitation appears to the north of R1,  
267 indicating an active atmospheric response to the SST warming over R1; whereas, there is an  
268 insignificant positive precipitation signal over R2 and its surrounding areas. Figure 6 further  
269 depicts that the SON SSTs over both R1 and R2 are positively correlated with  $AHD_{BTH}$ , and the  
270 TCC between the  $AHD_{BTH}$  and SON SST over R1 (R2) is 0.45 (0.28), exceeding the 99% (95%)  
271 confidence level. By virtue of the above analyses, we speculate that the SST over R1 may play a  
272 more important role than that over R2 in driving a higher  $AHD_{BTH}$ . Note, however, that when the  
273 SON SSTs over R1 and R2 are both obviously elevated, the  $AHD_{BTH}$  is more likely to be higher  
274 than normal, such as in 1980, 1987 and 2015. ~~Furthermore, a~~  $A_{SJ}$  indicated above, the  $AHD_{BTH}$  is  
275 closely correlated with the  $A_{SJ}$  and the associated air subsidence, which allows us to speculate that  
276 the positive SSTAs over R1 and R2 might drive the interannual variability of  $AHD_{BTH}$  by  
277 modulating the intensity of the  $A_{SJ}$  and associated subsidence. To validate this hypothesis, we  
278 firstly examine the pathway of SSTAs over R1 in driving  $AHD_{BTH}$ .

279 Figure 5c suggests that the SST warming in R1 may induce larger-area ~~concomitant~~ low-level  
280 easterly anomalies to its east, leading to anticyclonic wind shear over this region, which mainly  
281 ~~form over the southeastern portion of R1 and the area to its south~~. In such a scenario, an  
282 anticyclonic anomaly is induced (Fig. 5c), with its center to the northeast of R1. Along the western  
283 flank of this anticyclonic anomaly, warm and moist airflows move northwards. When these warm  
284 and moist airflows meet cold air mass in the areas to the north of R1, enhanced precipitation is  
285 thus generated (Fig. 5e). Meanwhile, the resultant enhanced rainfall condensation heating induces  
286 a cyclonic anomaly to its north, thereby exciting the other two pairs of the aforementioned  
287 teleconnection pattern along the westerly jet, as demonstrated by the Rossby wave train induced  
288 by SST warming in R1 (Figs. 7 and 8). Specifically, from the regressed SON UV850 (Fig. 7), we  
289 can see that the SST warming in R1 can indeed induce a significant low-level teleconnection  
290 pattern arising from the North Atlantic subtropics, bearing a close resemblance to that in Fig. 5c;  
291 and to the north of R1, where the rainfall condensation heating is triggered, the corresponding  
292 WAF exhibits a distinctive arc-shaped trajectory, perturbing the other two pairs of cyclones and  
293 anticyclones of the teleconnection (Fig. 8). This teleconnection extends from the North Atlantic  
294 towards Scandinavia, goes through the Eurasia and arrives at the Northeast Asia~~western North~~  
295 Pacific. Therefore, by means of this trajectory, Rossby wave energy in the middle (Fig. 8b) and  
296 upper (Fig. 8a) troposphere may propagate southeastwards into the  $A_{SJ}$  and its surrounding region,  
297 favoring the formation/sustainability of the  $A_{SJ}$  and the associated air subsidence. In this context,  
298 the associated meteorological parameters (Fig. S1), which resemble those tied to a higher  $AHD_{BTH}$   
299 (Fig. 4), might increase the likelihood of SON haze pollution over the BTH region. Again, this  
300 induced teleconnection is quasi-barotropic in structure, with its magnitude larger in the upper  
301 troposphere (Fig. 8a), which is consistent with that in Fig. 5a.

302 As for the role of~~When focusing on region~~ R2 SSTA warming (Fig. 9a), we find that,  
303 corresponding to the SSTAs over R2, there exists a cyclonic anomaly to the west of R2. Besides,  
304 substantial SSTA-induced low-level easterly anomalies are appeared to mainly located to the  
305 southeast of R2; ~~meanwhile~~plus, a large-scale~~huge~~ anticyclonic anomaly to the northeast is  
306 excited, with its center situated over the northern Pacific. In such a scenario, R2 is thoroughly  
307 ~~controlled~~penetrated by significant warm and humid airflows transported from the eastern flank of  
308 the cyclonic and the western flank of anticyclonic anomaly respectively (Fig. 9a), ~~warming the~~  
309 SST over R2. Furthermore, the airflow convergence primarily occurs over the southwestern  
310 portion of R2, where the strongly significant and positive rainfall anomaly is triggered (Fig. 9b).  
311 Thus, the enhanced significant rainfall heating ~~perturbation~~ may greatly intensify the ascending  
312 motion over R2 and the adjacent region, resulting in subsidence over the BTH region and  
313 Northeast Asia via an anomalous local meridional cell (Fig. 10a). As such, the BTH region ~~and its~~  
314 ~~adjacent areas are~~is dominated by significant warm temperatures in the middle and upper  
315 troposphere (Fig. 10b), ~~); leading to the maintenance and reinforcement of~~and the  $A_{SJ}$  ~~and~~ the  
316 downward motions over the BTH region; as well as the regional low-level stability over BTH, are  
317 maintained and reinforced. Under such circumstances, the vertical transport of APs is restricted  
318 (Zhang et al., 2014; Pei et al., 2018), and the near-surface winds are weakened (Li et al., 2016).  
319 ~~Meanwhile,~~ the parameters associated with SST warming in R2 (Fig. S2) also support the  
320 formation of haze weather over the BTH region.

## 322 4.2 Numerical model simulations

323 Two experiments were conducted to further validate the above-mentioned two pathways ~~in~~ of how  
324 SSTAs drive the variation of  $AHD_{BTH}$ . The first experiment (H\_NAS) simulated the responses to  
325 the heating induced by SSTAs over R1 (Fig. 11). H\_NAS was imposed with a specified heating

326 centered over the region to the north of R1 (center: 37.67°N, 64.69°W) that largely matched with  
327 the SON positive rainfall anomaly as shown in Fig. 5e. The second experiment (H\_WNP)  
328 mimicked the responses to the prescribed heating over the neighboring areas of R2 (center:  
329 15.35°N, 109.69°E; Fig. 12), where the corresponding regressed precipitation rate was the most  
330 significant ~~and amplified~~, as exhibited in Fig. 9b. The heating had a cosine-squared profile in an  
331 elliptical region in the horizontal direction. The maximum heating, with 1 K day<sup>-1</sup> amplitude, was  
332 set to be at 300 hPa.

333 Figure 11 presents the 200- and 500-hPa geopotential height and wind responses to the specified  
334 heating over the North Atlantic subtropical region. As anticipated, the equilibrium state (mean  
335 output from day 40 to day 60) of the Z200 (Fig. 11a) and Z500 (Fig. 11b) responses to the heating  
336 resembles the aforementioned teleconnection (Figs. 5a and 5b), and the simulated response of the  
337 Z200 anomalies is generally larger than its counterpart at 500 hPa (Fig. 11b), which concurs with  
338 the observational evidence. Besides, a similar low-level portion of the A<sub>SJ</sub> could also be simulated  
339 (figure not shown). As a result, a strengthened A<sub>SJ</sub> is induced.

340 Figure 12 delineates the 850-hPa geopotential height (Z850) and UV850 responses to the specified  
341 heating centered at (15.35°N, 109.69°E). Although there are some differences in spatial  
342 distribution compared with the observations, the well-organized cyclonic anomaly to the west of  
343 the heating center and the anticyclonic anomaly ~~over Northeast Asia to the north~~ can be ~~properly~~  
344 ~~well~~ simulated (Fig. 12). Meanwhile, the A<sub>SJ</sub> and the coherent tropospheric subsidence over the  
345 BTH region and the Northeast Asian anticyclonic anomaly were also simulated well (figure ~~not~~  
346 ~~shown/omitted~~), ~~leading to the amplified A<sub>SJ</sub> as well~~.

347 To sum up, from observational diagnoses and numerical simulations, we can conclude that there  
348 are two pathways regarding how ~~remote~~ SSTAs impact the formation and maintenance of the A<sub>SJ</sub>  
349 and the associated air subsidence. One pathway operates via a heating-induced large-scale  
350 teleconnection pattern arising from SST warming in R1, and the other is connected to an  
351 anomalous local meridional cell triggered by heating-reinforced ascending motion via local SST  
352 warming over R2.

353

354

## 355 5 Conclusions and discussion

356 Motivated by a lack of in-depth understanding with respect to the interannual variations of the  
357 AHD<sub>BTH</sub>, in the present study we explored the related climate anomalies (localized meteorological  
358 parameters, and large-scale atmospheric and oceanic anomalies) tied to the AHD<sub>BTH</sub>. We have  
359 substantiated that an above-normal AHD<sub>BTH</sub> is closely correlated with the simultaneous SST  
360 warming in two key regions (R1 over the North Atlantic subtropical sector, and R2 over the  
361 western North Pacific sector), and once the SON SST warming in R1 and R2 are both remarkably  
362 significant, their joint climate impacts can greatly enhance the likelihood of an above-normal  
363 AHD<sub>BTH</sub>.

364 Potential mechanisms associated with an above-normal AHD<sub>BTH</sub> have been proposed through  
365 further investigations. Since the A<sub>SJ</sub> and the associated subsidence over the A<sub>SJ</sub> and the  
366 surrounding region can yield meteorological circumstances conducive to enhancing the likelihood  
367 of haze pollution in the BTH region, the issue of an above-normal AHD<sub>BTH</sub> can be reasonably  
368 transferred into uncovering how the SON A<sub>SJ</sub> and associated air subsidence are developed and  
369 sustained. We found that there are two possible pathways. First, SST warming in R1 can induce a  
370 downstream Rossby wave teleconnection, and the associated Rossby wave energy can propagate

371 into ~~Northeast Asia~~  $A_{SJ}$  and its surrounding region through an arc-shaped trajectory,  
372 developing and strengthening the  $A_{SJ}$  and the associated subsidence over BTH. The other pathway,  
373 however, operates through localized heating-reinforced ascending motion over R2, also resulting  
374 in subsidence over the BTH region ~~and Northeast Asia~~ via an anomalous local meridional cell.

375 AGCM simulations ~~supported reinforced~~ our hypothesis. With prescribed heating over the region  
376 to the north of R1, a quite similar teleconnection—starting from the North Atlantic  
377 subtropics—was excited. If we imposed an idealized heating over the adjacent R2, where the  
378 corresponding precipitation rate was the most significant ~~and amplified~~, the ~~concomitant~~  
379 significant low-level convergence around the heated areas was simulated, ~~enhancing the SST~~  
380 ~~warming in R2 and~~ inducing the  $A_{SJ}$ -resembled circulation to the north and the subsidence over  
381 the BTH region ~~and Northeast Asia~~. However, because the model we used is an intermediate  
382 anomaly AGCM, and the heating prescribed in the model is idealized, the simulated patterns were  
383 slightly spatially different to those observed. Although the model cannot reproduce the  
384 geopotential height and wind anomalies perfectly, it can ~~nonetheless still~~ support ~~the our~~ proposed  
385 mechanisms. As a summary, a schematic illustration (Fig. 13) of the occurrence of a higher  
386  $AHD_{BTH}$  is provided, which encapsulates the major characteristics of the two pathways of how  
387 ~~remote~~ SSTAs over R1 and R2 drive the  $AHD_{BTH}$  respectively.

388 From the perspective of seasonal prediction, among all the previous individual months of boreal  
389 summer (June–July–August), the SON SST in R1 (R2) was most significantly correlated with the  
390 August SST in R1 (R2) on the interannual timescale, with a TCC of 0.35 (0.61) that exceeded the  
391 95% (99%) confidence level. This suggests that, when the August SST over R1 (R2) is higher, the  
392 subsequent SON SST over R1 (R2) is more likely to become warmer. As such, the previous  
393 August SSTA over R1 (R2) could serve as a possible precursor for the seasonal prediction of the  
394  $AHD_{BTH}$ .

395 In this study, we solely emphasize the potential impacts of SSTAs on the interannual variations of  
396 the  $AHD_{BTH}$ . It should be noted that other external forcings, such as the Arctic sea ice (e.g., Wang  
397 et al., 2015), Eurasian snowpack (e.g., Yin and Wang, 2018), thermal conditions on the Tibetan  
398 Plateau (e.g., Xu et al., 2016) and soil moisture (e.g., Yin and Wang, 2016b), may also exert  
399 profound impacts on haze pollution over China. Studying the mechanisms tied to these forcings  
400 may enhance the seasonal predicting skill for the  $AHD_{BTH}$ . Meanwhile, in this study, we only  
401 focus on the variability of  $AHD_{BTH}$  on interannual timescale. Whether the proposed mechanism of  
402  $AHD_{BTH}$  is still at play on intraseasonal timescale? Is it possible for making an extended-range  
403 forecast of the occurrence of haze days? ~~This-These is an important~~ topics are of both scientific  
404 and practical importance, and merit ~~deserving of~~ further explorations.

405

406

407 *Data availability.* The atmospheric data and land-surface data are available from the NCEP/NCAR data archive:  
408 <http://www.esrl.noaa.gov/psd/data/gridded/data.ncep.reanalysis.html> (NCEP/NCAR, 2018). The SST data were downloaded from  
409 <https://www.esrl.noaa.gov/psd/data/gridded/data.noaa.ersst.v5.html> (NOAA, 2018). The precipitation data were downloaded from  
410 <https://www.esrl.noaa.gov/psd/data/gridded/data.prec.html> (NOAA, 2018). The monthly PBLH data are available on the ERA-Interim  
411 website: <http://www.ecmwf.int/en/research/climate-reanalysis/era-interim> (ERA-Interim, 2018). The ground observations are from the  
412 National Meteorological Information Center of China (<http://data.cma.cn/>) (CMA, 2018).

413 *Competing interests.* The authors declare that they have no conflict of interest.

414 *Author contributions.* JW analyzed the observational data, ZZ and JW designed the numerical experiments. JW and ZZ wrote the

415 manuscript. LQ, QZ, JH and JXW were involved in the scientific interpretation and discussion.

416

417 *Acknowledgements.* This work was supported by the National Key Research and Development Program of China (Grants  
418 2018YFC1505905 and 2018YFC1505803), and the National Natural Science Foundation of China (Grants 41605035, ~~41371222,~~ and  
419 ~~41475086)~~ and the Priority Academic Program Development (PAPD) of Jiangsu Higher Education Institutions. Zhiwei was supported by  
420 ~~the Natural Science Foundation of Jiangsu Province (No. BK20161604) and the Startup Foundation for Introducing Talent of NUIST (No.~~  
421 ~~2018#026).~~

422

423

424

425

426

427

428

429

430

431

432

433

434

435

436

437

438

439

440

441

442

443

444

445

446

447

448

449

450

451

452

453

454

455

456

457

458

459 **References**

- 460 Cai, W. J., Li, K., Liao, H., Wang, H. J., and Wu, L. X.: Weather conditions conducive to Beijing severe haze more  
461 frequent under climate change, *Nat Clim Change*, 7, 257-262, 10.1038/nclimate3249, 2017.
- 462 Cao, J. J., Lee, S. C., Chow, J. C., Watson, J. G., Ho, K. F., Zhang, R. J., Jin, Z. D., Shen, Z. X., Chen, G. C., Kang,  
463 Y. M., Zou, S. C., Zhang, L. Z., Qi, S. H., Dai, M. H., Cheng, Y., and Hu, K.: Spatial and seasonal distributions  
464 of carbonaceous aerosols over China, *J Geophys Res Atmos*, 112, D22S11, 10.1029/2006JD008205, 2007.
- 465 Chameides, W. L., Yu, H., Liu, S. C., Bergin, M., Zhou, X., Mearns, L., Wang, G., Kiang, C. S., Saylor, R. D., Luo,  
466 C., Huang, Y., Steiner, A., and Giorgi, F.: Case study of the effects of atmospheric aerosols and regional haze on  
467 agriculture: An opportunity to enhance crop yields in China through emission controls?, *Proceedings of the*  
468 *National Academy of Sciences*, 96, 13626, 1999.
- 469 Charlson, R. J., Schwartz, S. E., Hales, J. M., Cess, R. D., Coakley Jr, J. A., Hansen, J. E., and Hofmann, D. J.:  
470 Climate forcing by anthropogenic aerosols, *Science*, 255, 423-430, 10.1126/science.255.5043.423, 1992.
- 471 Chen, H. P., and Wang, H. J.: Haze Days in North China and the associated atmospheric circulations based on daily  
472 visibility data from 1960 to 2012, *J Geophys Res Atmos*, 120, 5895-5909, 10.1002/2015JD023225, 2015.
- 473 Chen, J., Zhao, C. S., Ma, N., Liu, P. F., Göbel, T., Hallbauer, E., Deng, Z. Z., Ran, L., Xu, W. Y., Liang, Z., Liu, H.  
474 J., Yan, P., Zhou, X. J., and Wiedensohler, A.: A parameterization of low visibilities for hazy days in the North  
475 China Plain, *Atmos Chem Phys*, 12, 4935-4950, 10.5194/acp-12-4935-2012, 2012.
- 476 Chen, M. Y., Xie, P. P., Janowiak, J. E., and Arkin, P. A.: Global land precipitation: A 50-yr monthly analysis based  
477 on gauge observations, *J Hydrometeor*, 3, 249-266, 10.1175/1525-7541(2002)003<0249:glpaym>2.0.co;2, 2002.
- 478 Chen, Y. N., Zhu, Z. W., Luo, L., and Zhang, J. W.: Severe haze in Hangzhou in winter 2013/14 and associated  
479 meteorological anomalies, *Dyn Atmos Oceans*, 81, 73-83, 10.1016/j.dynatmoce.2018.01.002, 2018.
- 480 Chen, Y. Y., Ebenstein, A., Greenstone, M., and Li, H. B.: Evidence on the impact of sustained exposure to air  
481 pollution on life expectancy from China's Huai River policy, *Proc Natl Acad Sci*, 110, 12936-12941,  
482 10.1073/pnas.1300018110, 2013.
- 483 Chen, Z. Y., Xie, X. M., Cai, J., Chen, D. L., Gao, B. B., He, B., Cheng, N. L., and Xu, B.: Understanding  
484 meteorological influences on PM<sub>2.5</sub> concentrations across China: a temporal and spatial perspective, *Atmos*  
485 *Chem Phys*, 18, 5343-5358, 10.5194/acp-18-5343-2018, 2018.
- 486 Chung, C. E., Ramanathan, V., and Kiehl, J. T.: Effects of the South Asian absorbing haze on the Northeast  
487 monsoon and surface-air heat exchange, *J Climate*, 15, 2462-2476,  
488 10.1175/1520-0442(2002)015<2462:eotsaa>2.0.co;2, 2002.
- 489 CMA: China ground observation data sets, available at: <http://data.cma.cn/>, last access: 10 January 2018 (in  
490 Chinese).
- 491 Dee, D. P., Uppala, S. M., Simmons, A. J., Berrisford, P., Poli, P., Kobayashi, S., Andrae, U., Balmaseda, M. A.,  
492 Balsamo, G., Bauer, P., Bechtold, P., Beljaars, A. C. M., van de Berg, L., Bidlot, J., Bormann, N., Delsol, C.,  
493 Dragani, R., Fuentes, M., Geer, A. J., Haimberger, L., Healy, S. B., Hersbach, H., Hólm, E. V., Isaksen, I.,  
494 Kållberg, P., Köhler, M., Matricardi, M., McNally, A. P., Monge-Sanz, B. M., Morcrette, J. J., Park, B. K.,  
495 Peubey, C., de Rosnay, P., Tavolato, C., Thépaut, J. N., and Vitart, F.: The ERA-Interim reanalysis: configuration  
496 and performance of the data assimilation system, *Q J R Meteorol Soc*, 137, 553-597, 10.1002/qj.828, 2011.
- 497 Deser, C. and Michael S.T.: Atmosphere-ocean interaction on weekly timescales in the North Atlantic and Pacific.  
498 *Journal of Climate*, 10(3): 393-408, 1997.



499 Ding, Y. H., and Liu, Y. J.: Analysis of long-term variations of fog and haze in China in recent 50 years and their  
500 relations with atmospheric humidity, *Sci China Earth Sci*, 57, 36-46, 10.1007/s11430-013-4792-1, 2014.

501 Ding, Y. H., Wu, P., Liu, Y. J., and Song, Y. F.: Environmental and dynamic conditions for the occurrence of  
502 persistent haze events in North China, *Engineering*, 3, 266-271, 10.1016/J.ENG.2017.01.009, 2017.

503 ERA-Interim: PBLH data sets, available at: <http://www.ecmwf.int/en/research/climate-reanalysis/era-interim>, last  
504 access: 10 January 2018.

505 Gao, H., and Li, X.: Influences of El Nino Southern Oscillation events on haze frequency in eastern China during  
506 boreal winters, *Int J Climatol*, 35, 2682-2688, 10.1002/joc.4133, 2015.

507 Gao, Y., and Chen, D.: A dark October in Beijing 2016, *Atmos Oceanic Sci Lett*, 10, 206-213,  
508 10.1080/16742834.2017.1293473, 2017.

509 Guo, J. P., Zhang, X. Y., Wu, Y. R., Zhaxi, Y. Z., Che, H. Z., La, B., Wang, W., and Li, X. W.: Spatio-temporal  
510 variation trends of satellite-based aerosol optical depth in China during 1980–2008, *Atmos Environ*, 45,  
511 6802-6811, 10.1016/j.atmosenv.2011.03.068, 2011.

512 Guo, S., Hu, M., Zamora, M. L., Peng, J. F., Shang, D. J., Zheng, J., Du, Z. F., Wu, Z. J., Shao, M., Zeng, L. M.,  
513 Molina, M. J., and Zhang, R. Y.: Elucidating severe urban haze formation in China, *Proc Natl Acad Sci*, 111,  
514 17373-17378, 10.1073/pnas.1419604111, 2014.

515 He, J. H., and Zhu, Z. W.: The relation of South China Sea monsoon onset with the subsequent rainfall over the  
516 subtropical East Asia, *Int J Climatol*, 35, 4547-4556, 10.1002/joc.4305, 2015.

517 Held, I. M., and Suarez, M. J.: A proposal for the intercomparison of the dynamical cores of atmospheric general  
518 circulation models, *Bull Amer Meteor Soc*, 75, 1825-1830, 10.1175/1520-0477(1994)075<1825:apftio>2.0.co;2,  
519 1994.

520 Huang, B. Y., Thorne, P. W., Banzon, V. F., Boyer, T., Chepurin, G., Lawrimore, J. H., Menne, M. J., Smith, T. M.,  
521 Vose, R. S., and Zhang, H. M.: Extended Reconstructed Sea Surface Temperature, version 5 (ERSSTv5):  
522 Upgrades, validations, and intercomparisons, *J Climate*, 30, 8179-8205, 10.1175/jcli-d-16-0836.1, 2017.

523 [Hurrell, J. W., and Deser, C.: North Atlantic climate variability: The role of the North Atlantic Oscillation, \*J\*](#)  
524 [Marine Syst](#), 78, 28-41, 10.1016/j.jmarsys.2008.11.026, 2009.

525 Jacob, D. J., and Winner, D. A.: Effect of Climate Change on Air Quality, *Atmos Environ*, 43, 51-63,  
526 10.1016/j.atmosenv.2008.09.051, 2009.

527 Jia, B., Wang, Y., Yao, Y., and Xie, Y.: A new indicator on the impact of large-scale circulation on wintertime  
528 particulate matter pollution over China, *Atmos Chem Phys*, 15, 11919-11929, 10.5194/acp-15-11919-2015,  
529 2015.

530 Kalnay, E., Kanamitsu, M., Kistler, R., Collins, W., Deaven, D., Gandin, L., Iredell, M., Saha, S., White, G.,  
531 Woollen, J., Zhu, Y., Leetmaa, A., Reynolds, R., Chelliah, M., Ebisuzaki, W., Higgins, W., Janowiak, J., Mo, K.  
532 C., Ropelewski, C., Wang, J., Jenne, R., and Joseph, D.: The NCEP/NCAR 40-year reanalysis project, *Bull*  
533 *Amer Meteor Soc*, 77, 437-471, 10.1175/1520-0477(1996)077<0437:tnyrp>2.0.co;2, 1996.

534 Lau, K. M., and Kim, K. M.: Observational relationships between aerosol and Asian monsoon rainfall, and  
535 circulation, *Geophys Res Lett*, 33, L21810, 10.1029/2006GL027546, 2006.

536 Lau, K. M., Kim, M. K., and Kim, K. M.: Asian summer monsoon anomalies induced by aerosol direct forcing: the  
537 role of the Tibetan Plateau, *Clim Dyn*, 26, 855-864, 10.1007/s00382-006-0114-z, 2006.

- 538 Li, C., Martin, R. V., Boys, B. L., van Donkelaar, A., and Ruzzante, S.: Evaluation and application of multi-decadal  
539 visibility data for trend analysis of atmospheric haze, *Atmos Chem Phys*, 16, 2435-2457,  
540 10.5194/acp-16-2435-2016, 2016.
- 541 Li, Q., Zhang, R. H., and Wang, Y.: Interannual variation of the wintertime fog–haze days across central and  
542 eastern China and its relation with East Asian winter monsoon, *Int J Climatol*, 36, 346-354, 10.1002/joc.4350,  
543 2016.
- 544 Li, R., Hu, Y. J., Li, L., Fu, H. B., and Chen, J. M.: Real-time aerosol optical properties, morphology and mixing  
545 states under clear, haze and fog episodes in the summer of urban Beijing, *Atmos Chem Phys*, 17, 5079-5093,  
546 10.5194/acp-17-5079-2017, 2017.
- 547 Li, Z. Q., Lau, W. K. M., Ramanathan, V., Wu, G., Ding, Y., Manoj, M. G., Liu, J., Qian, Y., Li, J., Zhou, T., Fan, J.,  
548 Rosenfeld, D., Ming, Y., Wang, Y., Huang, J., Wang, B., Xu, X., Lee, S. S., Cribb, M., Zhang, F., Yang, X., Zhao,  
549 C., Takemura, T., Wang, K., Xia, X., Yin, Y., Zhang, H., Guo, J., Zhai, P. M., Sugimoto, N., Babu, S. S., and  
550 Brasseur, G. P.: Aerosol and monsoon climate interactions over Asia, *Rev Geophys*, 54, 866-929,  
551 10.1002/2015RG000500, 2016.
- 552 Liu, Y., Sun, J. R., and Yang, B.: The effects of black carbon and sulphate aerosols in China regions on East Asia  
553 monsoons, *Tellus B*, 61, 642-656, 10.1111/j.1600-0889.2009.00427.x, 2009.
- 554 Luan, T., Guo, X. L., Guo, L. J., and Zhang, T. H.: Quantifying the relationship between PM<sub>2.5</sub> concentration,  
555 visibility and planetary boundary layer height for long-lasting haze and fog–haze mixed events in Beijing,  
556 *Atmos Chem Phys*, 18, 203-225, 10.5194/acp-18-203-2018, 2018.
- 557 Mu, M., and Zhang, R. H.: Addressing the issue of fog and haze: A promising perspective from meteorological  
558 science and technology, *Sci China Earth Sci*, 57, 1-2, 10.1007/s11430-013-4791-2, 2014.
- 559 Mu, Q., and Liao, H.: Simulation of the interannual variations of aerosols in China: role of variations in  
560 meteorological parameters, *Atmos Chem Phys*, 14, 9597-9612, 10.5194/acp-14-9597-2014, 2014.
- 561 NCEP/NCAR: NCEP/NCAR Reanalysis data sets, available at: <http://www.esrl.noaa.gov/psd/data>  
562 [/gridded/data.ncep.reanalysis.html](http://www.esrl.noaa.gov/psd/data/gridded/data.ncep.reanalysis.html), last access: 10 January 2018.
- 563 Niu, F., Li, Z. Q., Li, C., Lee, K. H., and Wang, M. Y.: Increase of wintertime fog in China: Potential impacts of  
564 weakening of the Eastern Asian monsoon circulation and increasing aerosol loading, *J Geophys Res*, 115,  
565 D00K20, 10.1029/2009JD013484, 2010.
- 566 NOAA: NOAA Extended Reconstructed Sea Surface Temperature (SST) V5 data sets, available at:  
567 <https://www.esrl.noaa.gov/psd/data/gridded/data.noaa.ersst.v5.html>, last access: 10 January 2018.
- 568 NOAA: NOAA precipitation datasets, available at: <https://www.esrl.noaa.gov/psd/data/gridded/data.prec.html>,  
569 last access: 10 January 2018.
- 570 Pei, L., Yan, Z. W., Sun, Z. B., Miao, S. G., and Yao, Y.: Increasing persistent haze in Beijing: potential impacts of  
571 weakening East Asian winter monsoons associated with northwestern Pacific sea surface temperature trends,  
572 *Atmos Chem Phys*, 18, 3173–3183, 10.5194/acp-18-3173-2018, 2018.
- 573 Pope III, C. A., and Dockery, D. W.: Health effects of fine particulate air pollution: Lines that connect, *J Air Waste*  
574 *Manage*, 56, 709-742, 10.1080/10473289.2006.10464485, 2006.
- 575 Seo, J., Kim, J. Y., Youn, D., Lee, J. Y., Kim, H., Lim, Y. B., Kim, Y., and Jin, H. C.: On the multiday haze in the  
576 Asian continental outflow: the important role of synoptic conditions combined with regional and local sources,  
577 *Atmos Chem Phys*, 17, 9311-9332, 10.5194/acp-17-9311-2017, 2017.

578 Takaya, K., and Nakamura, H.: A formulation of a phase-independent wave-activity flux for stationary and  
579 migratory quasigeostrophic eddies on a zonally varying basic flow, *J Atmos Sci*, 58, 608-627,  
580 10.1175/1520-0469(2001)058<0608:afopi>2.0.co;2, 2001.

581 Tao, M. H., Chen, L. F., Xiong, X. Z., Zhang, M. G., Ma, P. F., Tao, J. H., and Wang, Z. F.: Formation process of  
582 the widespread extreme haze pollution over northern China in January 2013: Implications for regional air  
583 quality and climate, *Atmos Environ*, 98, 417-425, 10.1016/j.atmosenv.2014.09.026, 2014.

584 Tao, M. H., Chen, L. F., Wang, Z. F., Wang, J., Tao, J. H., and Wang, X. H.: Did the widespread haze pollution over  
585 China increase during the last decade? A satellite view from space, *Environ Res Lett*, 11, 054019,  
586 10.1088/1748-9326/11/5/054019, 2016.

587 Tett, S. F. B., Stott, P. A., Allen, M. R., Ingram, W. J., and Mitchell, J. F. B.: Causes of twentieth-century  
588 temperature change near the Earth's surface, *Nature*, 399, 569-572, 10.1038/21164, 1999

589 Tie, X. X., Wu, D., and Brasseur, G.: Lung cancer mortality and exposure to atmospheric aerosol particles  
590 in Guangzhou, China, *Atmos Environ*, 43, 2375-2377, 10.1016/j.atmosenv.2009.01.036, 2009.

591 Wang, H. J., Chen, H. P., and Liu, J. P.: Arctic sea ice decline intensified haze pollution in eastern China, *Atmos*  
592 *Oceanic Sci Lett*, 8, 1-9, 10.3878/AOSL20140081, 2015.

593 Wang, H. J., and Chen, H. P.: Understanding the recent trend of haze pollution in eastern China: roles of climate  
594 change, *Atmos Chem Phys*, 16, 4205-4211, 10.5194/acp-16-4205-2016, 2016.

595 Wang, H. J.: On assessing haze attribution and control measures in China, *Atmos Oceanic Sci Lett*, 11, 120-122,  
596 10.1080/16742834.2018.1409067, 2018.

597 Wang, J., He, J. H., Liu, X. F., and Wu, B. G.: Interannual variability of the Meiyu onset over Yangtze-Huaihe  
598 River Valley and analyses of its previous strong influence signal, *Chin Sci Bull*, 54, 687-695,  
599 10.1007/s11434-008-0534-8, 2009.

600 Wang, J., Zhang, X. Y., Cai, Z. Y., Wang, D. Z., and Chen, H.: Meteorological causes of a heavy air pollution  
601 process in Tianjin and its prediction analyses, *Environ Sci Technol*, 38, 77-82, 2015 (in Chinese).

602 Wang, J., Zhao, Q. H., Zhu, Z. W., Qi, L., Wang, J. X. L., and He, J. H.: Interannual variation in the number and  
603 severity of autumnal haze days in the Beijing–Tianjin–Hebei region and associated atmospheric circulation  
604 anomalies, *Dyn Atmos Oceans*, 84, 1-9, 10.1016/j.dynatmoce.2018.08.001, 2018.

605 Wang, Y. S., Yao, L., Wang, L. L., Liu, Z. R., Ji, D. S., Tang, G. Q., Zhang, J. K., Sun, Y., Hu, B., and Xin, J. Y.:  
606 Mechanism for the formation of the January 2013 heavy haze pollution episode over central and eastern China,  
607 *Sci China Earth Sci*, 57, 14-25, 10.1007/s11430-013-4773-4, 2014.

608 Wang, Z. F., Li, J., Wang, Z., Yang, W. Y., Tang, X., Ge, B. Z., Yan, P. Z., Zhu, L. L., Chen, X. S., Chen, H. S.,  
609 Wang, W., Li, J. J., Liu, B., Wang, X. Y., Wang, W., Zhao, Y. L., Lu, N., and Su, D. B.: Modeling study of  
610 regional severe hazes over mid-eastern China in January 2013 and its implications on pollution prevention and  
611 control, *Sci China Earth Sci*, 57, 3-13, 10.1007/s11430-013-4793-0, 2014.

612 Wu, D., Tie, X. X., Li, C. C., Ying, Z. M., Kai-Hon Lau, A., Huang, J., Deng, X. J., and Bi, X. Y.: An extremely  
613 low visibility event over the Guangzhou region: A case study, *Atmos Environ*, 39, 6568-6577,  
614 10.1016/j.atmosenv.2005.07.061, 2005.

615 Wu, G. X., Li, Z. Q., Fu, C. B., Zhang, X. Y., Zhang, R. Y., Zhang, R. H., Zhou, T. J., Li, J. P., Li, J. D., Zhou, D.  
616 G., Wu, L., Zhou, L. T., He, B., and Huang, R. H.: Advances in studying interactions between aerosols and  
617 monsoon in China, *Sci China Earth Sci*, 59, 1-16, 10.1007/s11430-015-5198-z, 2016.

- 618 Xiao, D., Li, Y., Fan, S. J., Zhang, R. H., Sun, J. R., and Wang, Y.: Plausible influence of Atlantic Ocean SST  
619 anomalies on winter haze in China, *Theor Appl Climatol*, 122, 249-257, 10.1007/s00704-014-1297-6, 2015.
- 620 Xu, P., Chen, Y. F., and Ye, X. J.: Haze, air pollution, and health in China, *Lancet*, 382, 2067,  
621 10.1016/S0140-6736(13)62693-8, 2013.
- 622 Xu, X., Zhao, T., Liu, F., Gong, S. L., Kristovich, D., Lu, C., Guo, Y., Cheng, X., Wang, Y., and Ding, G.: Climate  
623 modulation of the Tibetan Plateau on haze in China, *Atmos Chem Phys*, 16, 1365-1375,  
624 10.5194/acp-16-1365-2016, 2016.
- 625 Xu, X. D., Wang, Y. J., Zhao, T. L., Cheng, X. H., Meng, Y. Y., and Ding, G. A.: “Harbor” effect of large  
626 topography on haze distribution in eastern China and its climate modulation on decadal variations in haze China ,  
627 *Chin Sci Bull*, 60, 1132-1143, 10.1360/N972014-00101, 2015 (in Chinese).
- 628 Yang, Y., Liao, H., and Lou, S. J.: Decadal trend and interannual variation of outflow of aerosols from East Asia:  
629 Roles of variations in meteorological parameters and emissions, *Atmos Environ*, 100, 141-153,  
630 10.1016/j.atmosenv.2014.11.004, 2015.
- 631 Yang, Y., Liao, H., and Lou, S. J.: Increase in winter haze over eastern China in recent decades: Roles of variations  
632 in meteorological parameters and anthropogenic emissions, *J Geophys Res Atmos*, 121, 13,050-013,065,  
633 10.1002/2016JD025136, 2016.
- 634 Yang, Y. R., Liu, X. G., Qu, Y., An, J. L., Jiang, R., Zhang, Y. H., Sun, Y. L., Wu, Z. J., Zhang, F., Xu, W. Q., and  
635 Ma, Q. X.: Characteristics and formation mechanism of continuous hazes in China: a case study during the  
636 autumn of 2014 in the North China Plain, *Atmos Chem Phys*, 15, 8165-8178, 10.5194/acp-15-8165-2015, 2015.
- 637 ~~Yin, Z. C., Wang, H. J., and Guo, W. L.: Climatic change features of fog and haze in winter over North China and  
638 Huang Huai Area, *Sci China Earth Sci*, 58, 1370-1376, 10.1007/s11430-015-5089-3, 2015.~~
- 639 ~~Yin, Z. C., and Wang, H. J.: The relationship between the subtropical Western Pacific SST and haze over  
640 North-Central North China Plain, *Int J Climatol*, 36, 3479-3491, 10.1002/joc.4570, 2016a.~~
- 641 Yin, Z. C., and Wang, H. J.: Seasonal prediction of winter haze days in the north central North China Plain, *Atmos  
642 Chem Phys*, 16, 14843-14852, 10.5194/acp-16-14843-2016, 2016b.
- 643 ~~Yin, Z. C., and Wang, H. J.: Role of atmospheric circulations in haze pollution in December 2016, *Atmos Chem  
644 Phys*, 17, 11673-11681, 10.5194/acp-17-11673-2017, 2017.~~
- 645 Yin, Z. C., Wang, H. J., and Chen, H. P.: Understanding severe winter haze events in the North China Plain in 2014:  
646 roles of climate anomalies, *Atmos Chem Phys*, 17, 1641-1651, 10.5194/acp-17-1641-2017, 2017.
- 647 ~~Yin, Z. C., and Wang, H. J.: The strengthening relationship between Eurasian snow cover and December haze days  
648 in central North China after the mid-1990s, *Atmos Chem Phys*, 18, 4753-4763, 10.5194/acp-18-4753-2018,  
649 2018.~~
- 650 You, T., Wu, R. G., Huang, G., and Fan, G. Z.: Regional meteorological patterns for heavy pollution events in  
651 Beijing, *J Meteor Res*, 31, 597-611, 10.1007/s13351-017-6143-1, 2017.
- 652 ~~You, Y. C., Cheng, X. G., Zhao, T. L., Xu, X. D., Gong, S. L., Zhang, X. Y., Zheng, Y., Che, H. Z., Yu, C., Chang, J.  
653 C., Ma, G. X., and Wu, M.: Variations of haze pollution in China modulated by thermal forcing of the Western  
654 Pacific Warm Pool, *Atmosphere*, 9, 314, 10.3390/atmos9080314, 2018.~~
- 655 Zhang, H., Zhao, S. Y., Wang, Z. L., Zhang, X. Y., and Song, L. C.: The updated effective radiative forcing of  
656 major anthropogenic aerosols and their effects on global climate at present and in the future, *Int J Climatol*, 36,

657 4029-4044, 10.1002/joc.4613, 2016.

658 Zhang, L., Wang, T., Lv, M. Y., and Zhang, Q.: On the severe haze in Beijing during January 2013: Unraveling the  
659 effects of meteorological anomalies with WRF-Chem, *Atmos Environ*, 104, 11-21,  
660 10.1016/j.atmosenv.2015.01.001, 2015.

661 Zhang, R. H., Li, Q., and Zhang, R. N.: Meteorological conditions for the persistent severe fog and haze event over  
662 eastern China in January 2013, *Sci China Earth Sci*, 57, 26-35, 10.1007/s11430-013-4774-3, 2014.

663 Zhang, Z. Y., Zhang, X., Gong, D. Y., Kim, S. J., Mao, R., and Zhao, X.: Possible influence of atmospheric  
664 circulations on winter haze pollution in the Beijing–Tianjin–Hebei region, northern China, *Atmos Chem Phys*,  
665 16, 561-571, 10.5194/acp-16-561-2016, 2016.

666 Zhao, S. Y., Zhang, H., and Xie, B.: The effects of El Niño–Southern Oscillation on the winter haze pollution of  
667 China, *Atmos Chem Phys*, 18, 1863–1877, 10.5194/acp-18-1863-2018, 2018.

668 Zhu, X. W., Tang, G. Q., Hu, B., Wang, L. L., Xin, J. Y., Zhang, J. K., Liu, Z. R., Munkel, C., and Wang, Y. S.:  
669 Regional pollution and its formation mechanism over North China Plain: A case study with ceilometer  
670 observations and model simulations, *J Geophys Res Atmos*, 121, 14574-14588, 10.1002/2016JD025730, 2016.

671 Zhu, Z. W., Li, T., and He, J. H.: Out-of-Phase relationship between boreal spring and summer decadal rainfall  
672 changes in southern China, *J Climate*, 27, 1083-1099, 10.1175/jcli-d-13-00180.1, 2014.

673 Zhu, Z. W., and Li, T.: A new paradigm for continental U.S. summer rainfall variability: Asia–North America  
674 teleconnection, *J Climate*, 29, 7313-7327, 10.1175/jcli-d-16-0137.1, 2016.

675 Zhu, Z. W., and Li, T.: The record-breaking hot summer in 2015 over Hawaii and its physical causes, *J Climate*, 30,  
676 4253-4266, 10.1175/JCLI-D-16-0438.1, 2017.

677 Zhu, Z. W.: Breakdown of the relationship between Australian summer rainfall and ENSO caused by tropical  
678 Indian Ocean SST warming, *J Climate*, 31, 2321-2336, 10.1175/jcli-d-17-0132.1, 2018.

679 Zhu, Z. W., and Li, T.: Amplified contiguous United States summer rainfall variability induced by East Asian  
680 monsoon interdecadal change, *Clim Dyn*, 50, 3523-3536, 10.1007/s00382-017-3821-8, 2018.

681 Zou, Y. F., Wang, Y. H., Zhang, Y. Z., and Koo, J.-H.: Arctic sea ice, Eurasia snow, and extreme winter haze in  
682 China, *Sci Adv*, 3, e1602751, 10.1126/sciadv.1602751, 2017.

683  
684  
685  
686  
687  
688  
689  
690  
691  
692  
693  
694  
695  
696  
697

## 698 Figures Captions

699 **Figure 1.** Topographic map (shaded; m) for the BTH region and the locations of 20 meteorological sites (colored dots). The dots colored  
700 red (light red; magenta) represent significant positive temporal correlation coefficients at the 99% (95%; 90%) confidence level between  
701 the  $AHD_{BTH}$  and AHD for every individual site on the interannual timescale.

702 **Figure 2.** Time series of the raw  $AHD_{BTH}$  (black line; days), along with its interdecadal component (blue line; days) and interannual  
703 component (red line; days), for the period 1960–2017. The gray horizontal line delineates the average climate value of the raw  $AHD_{BTH}$   
704 during 1960–2017.

705 **Figure 3.** The climatological-mean (1960–2017) autumnal (a) Z500 (contours; gpm), UV850 (vectors;  $m s^{-1}$ ) and total cloud (shaded; %),  
706 and (b) surface relative humidity (shaded; %) and surface air temperature (contours;  $^{\circ}C$ ). The gray shaded area denotes the Tibetan  
707 Plateau, and the blue dashed box delineates the research domain of the BTH region. The letter A represents the center of anticyclonic  
708 circulation.

709 **Figure 4.** Regressed patterns of autumnal meteorological parameters onto the interannual component of the  $AHD_{BTH}$ , including (a)  
710 surface relative humidity (shaded; %), (b) surface air temperature (shaded;  $^{\circ}C$ ), (c) surface wind speed (shaded;  $m s^{-1}$ ), (d) SLP (shaded;  
711 hPa), (e) PBLH (shaded; m), and (f) 500-hPa omega (shaded;  $10^{-2} Pa s^{-1}$ ). Regression coefficients that are significant at the 90%  
712 confidence level are stippled. The blue dashed box outlines the research domain of the BTH region.

713 **Figure 5.** Regressed anomalies of autumnal (a) 200-hPa geopotential height (Z200; shaded; gpm) and 200-hPa winds (UV200; vectors;  $m$   
714  $s^{-1}$ ), (b) Z500 (shaded; gpm) and 500-hPa winds (UV500; vectors;  $m s^{-1}$ ), (c) SST (shaded;  $^{\circ}C$ ) and UV850 (vectors;  $m s^{-1}$ ), (d) SLP  
715 (shaded; hPa) and surface winds (vectors;  $m s^{-1}$ ), and (e) precipitation (shaded;  $mm day^{-1}$ ), with respect to the interannual component of  
716 the  $AHD_{BTH}$ . Regression coefficients that are significant at the 95% (90%) confidence level are stippled (cross hatched). In panels (a) and  
717 (b), only the wind vectors with statistical significance above the 90% confidence level are shown. In panel (c), the two red dashed  
718 rectangles, labelled R1 and R2, are the key regions where SSTAs are significantly correlated with the interannual component of the  
719  $AHD_{BTH}$ ; vectors with scales less than  $0.05 m s^{-1}$  are omitted. In panel (d), vectors with scales less than  $0.03 m s^{-1}$  are omitted. The blue  
720 dashed box delineates the research domain of the BTH region. The letters A and C represent the centers of anticyclonic and cyclonic  
721 anomalies, respectively.

722 **Figure 6.** Time series of the normalized interannual component of the  $AHD_{BTH}$  (black line), along with the simultaneous SST over R1  
723 (red line) and R2 (blue line) for the period 1960–2017. The horizontal dashed lines denote 0.8 of the standard deviation. The numerals  
724 labelled at the bottom represent the correlation coefficients ( $r$ ) between the  $AHD_{BTH}$  and simultaneous SST over R1 and R2, separately.  
725 The upper and lower dots in the red line indicate the three highest and lowest years of SST over R1, respectively.

726 **Figure 7.** Regressed anomalies of autumnal UV850 (vectors;  $m s^{-1}$ ) with respect to the simultaneous interannual component of the SST  
727 over R1. Green arrows represent the wind vectors with statistical significance above the 90% confidence level. The red dashed rectangle  
728 labelled R1 is the key region where SSTAs are significantly correlated with the interannual component of the  $AHD_{BTH}$ . The blue dashed  
729 box delineates the research domain of the BTH region. The gray shaded area denotes the Tibetan Plateau. The letters A and C represent  
730 the centers of anticyclonic and cyclonic anomalies, respectively.

731 **Figure 8.** The autumnal composite differences of (a) 200-hPa and (b) 500-hPa WAF (vectors;  $m^2 s^{-2}$ ), geopotential height (contours;  
732 gpm), and relative vorticity (shaded;  $10^{-5} s^{-1}$ ) between the three highest and three lowest years of simultaneous SST over R1 (highest  
733 minus lowest), as shown in Fig. 6. The red dashed rectangle labelled R1 is the key region where SSTAs are significantly correlated with  
734 the interannual component of the  $AHD_{BTH}$ . The blue dashed box delineates the research domain of the BTH region.

735 **Figure 9.** Regressed anomalies of autumnal (a) UV850 (vectors;  $m s^{-1}$ ) and SST (shaded;  $^{\circ}C$ ), and (b) precipitation (shaded;  $mm day^{-1}$ )  
736 with respect to the simultaneous interannual component of the SST over R2. In panel (a), green arrows represent the wind vectors with  
737 statistical significance above the 99% confidence level, and vectors with scales less than  $0.05 m s^{-1}$  are omitted. Regression coefficients  
738 that are significant at the 99% confidence level are cross hatched. The dashed red rectangle labelled R2 is the key region where SSTAs are  
739 significantly correlated with the interannual component of the  $AHD_{BTH}$ . The blue dashed box delineates the research domain of the BTH  
740 region. The gray shaded area denotes the Tibetan Plateau. The letter A (C) represents the center of anticyclonic (cyclonic) anomaly.

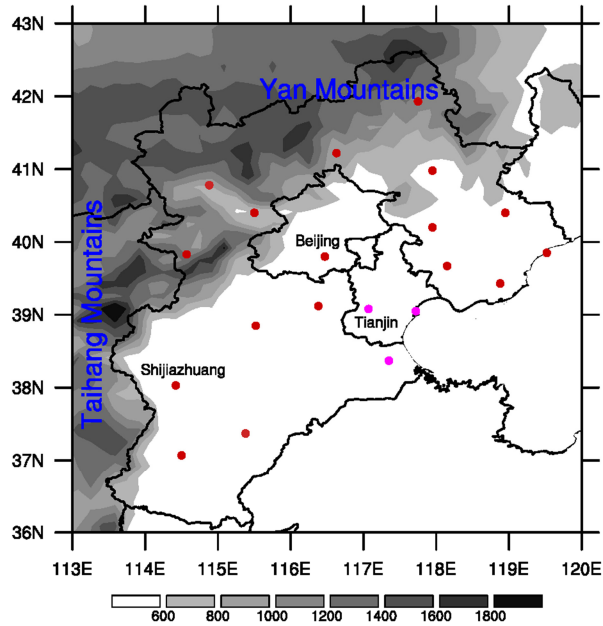
741 **Figure 10.** (a) Latitude–vertical section ( $112.5^{\circ}$ – $130^{\circ}E$ ) of the autumnal omega (shaded;  $10^{-2} Pa s^{-1}$ ) and (b) longitude–vertical section  
742 ( $35^{\circ}$ – $42.5^{\circ}N$ ) of the autumnal air temperature (shaded;  $^{\circ}C$ ) anomalies regressed onto the simultaneous interannual component of the SST  
743 over R2. Regression coefficients that are significant at the 90% confidence level are stippled. The thick blue horizontal bars superimposed  
744 onto the abscissa of panels (a) and (b) indicate the latitudes and longitudes of the BTH region, respectively.

745 **Figure 11.** The response of anomalous (a) Z200 (shaded; 10 gpm) and UV200 (vectors;  $m s^{-1}$ ), and (b) Z500 (shaded; 10 gpm) and  
746 UV500 (vectors;  $m s^{-1}$ ) in  $H\_NAS$ . The red contours indicate the imposed idealized heating. The blue dashed box delineates the research  
747 domain of the BTH region. The letters A and C represent the centers of anticyclonic and cyclonic anomalies, respectively.

748 **Figure 12.** The response of Z850 (shaded; 10 gpm) and UV850 (vectors;  $m s^{-1}$ ) in  $H\_WNP$ . The magenta contours indicate the imposed  
749 idealized heating. The blue dashed box delineates the research domain of the BTH region. The gray shaded area denotes the Tibetan  
750 Plateau. The letter A (C) represents the center of anticyclonic (cyclonic) anomaly.

751 **Figure 13.** Schematic diagram encapsulating the SSTA-induced (warming in R1 and R2) physical mechanisms and pathways connected  
752 to above-normal  $AHD_{BTH}$  years on the interannual timescale. Anomalous quasi-barotropic anticyclones (A) and cyclones (C) are indicated  
753 by blue and red elliptical cycles with arrows separately, denoting large-scale Rossby wave train triggered by the heating to the north of R1.  
754 Green arrows depict the key horizontal low-level (850-hPa) airflows. The red, azure and green arrows together exhibit the vertical  
755 overturning circulation tied to the SST warming in R2. The left-hand (right-hand) side of the cloud-resembled pattern with violet short  
756 dashed lines presents the significant anomalous precipitation induced by SSTAs over R1 (R2). The blue dashed box delineates the  
757 research domain of the BTH region.

758



759

760 **Figure 1.** Topographic map (shaded; m) for the BTH region and the locations of 20 meteorological sites (colored dots). The dots colored  
 761 red (light red; magenta) represent significant positive temporal correlation coefficients at the 99% (95%; 90%) confidence level between  
 762 the  $AHD_{BTH}$  and AHD for every individual site on the interannual timescale.

763

764

765

766

767

768

769

770

771

772

773

774

775

776

777

778

779

780

781

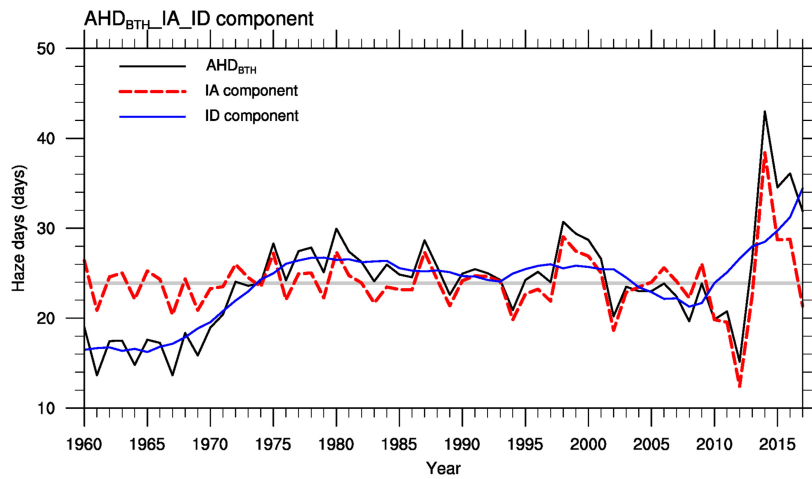
782

783

784

785

786

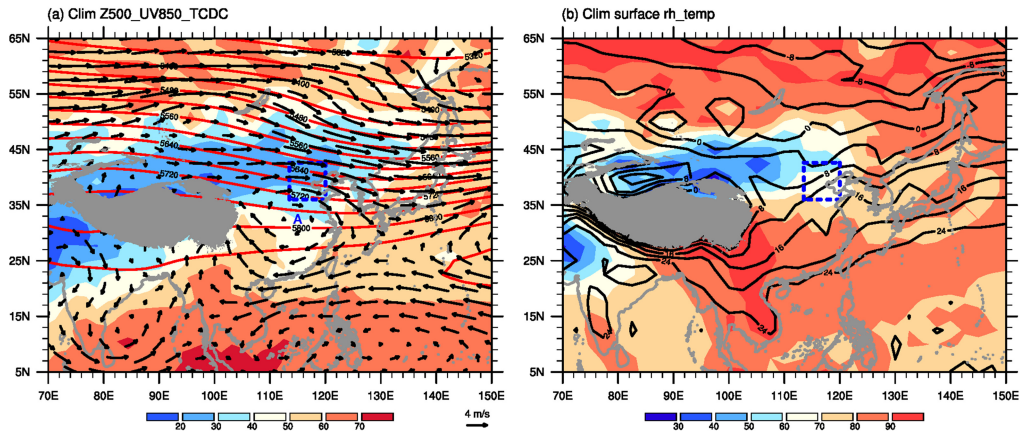


787

788 **Figure 2.** Time series of the raw AHD<sub>BTH</sub> (black line; days), along with its interdecadal component (blue line; days) and interannual  
 789 component (red line; days), for the period 1960–2017. The gray horizontal line delineates the average climate value of the raw AHD<sub>BTH</sub>  
 790 during 1960–2017.

791  
 792  
 793  
 794  
 795  
 796  
 797  
 798  
 799  
 800  
 801  
 802  
 803  
 804  
 805  
 806  
 807  
 808  
 809  
 810  
 811  
 812  
 813  
 814  
 815  
 816  
 817





818

819 **Figure 3.** The climatological-mean (1960–2017) autumnal (a) Z500 (contours; gpm), UV850 (vectors;  $m\ s^{-1}$ ) and total cloud (shaded; %),  
 820 and (b) surface relative humidity (shaded; %) and surface air temperature (contours;  $^{\circ}C$ ). The gray shaded area denotes the Tibetan  
 821 Plateau, and the blue dashed box delineates the research domain of the BTH region. The letter A represents the center of anticyclonic  
 822 circulation.

823

824

825

826

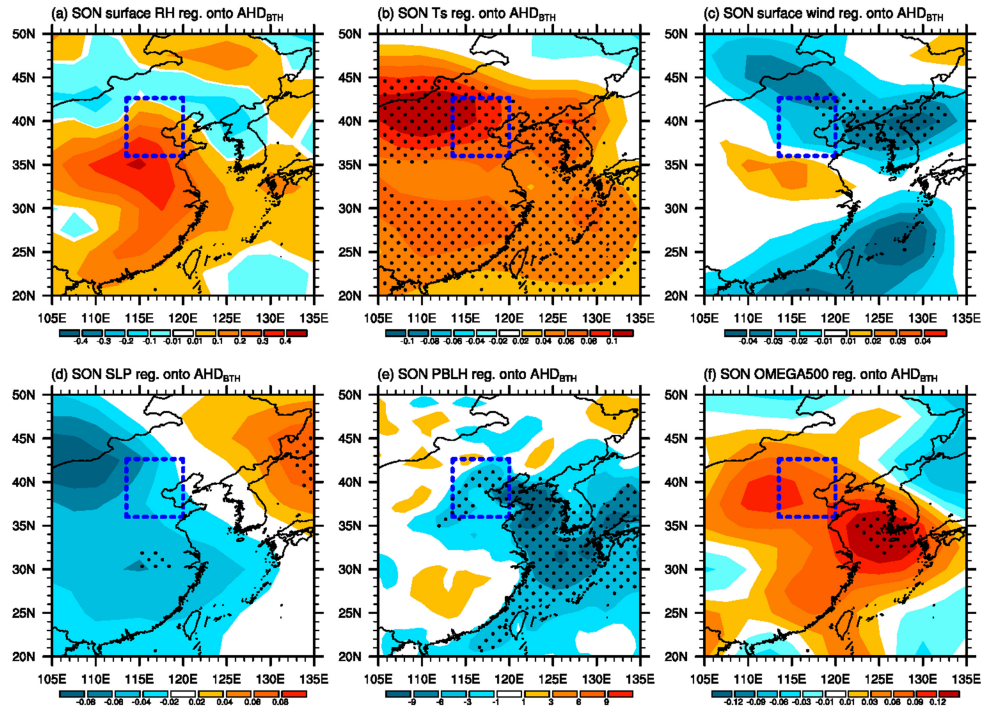
827

828

829

830

831



832

833 **Figure 4.** Regressed patterns of autumnal meteorological parameters onto the interannual component of the  $AHD_{BTH}$ , including (a)  
 834 surface relative humidity (shaded; %), (b) surface air temperature (shaded;  $^{\circ}C$ ), (c) surface wind speed (shaded;  $m s^{-1}$ ), (d) SLP (shaded;  
 835 hPa), (e) PBLH (shaded; m), and (f) 500-hPa omega (shaded;  $10^{-2} Pa s^{-1}$ ). Regression coefficients that are significant at the 90%  
 836 confidence level are stippled. The blue dashed box outlines the research domain of the BTH region.

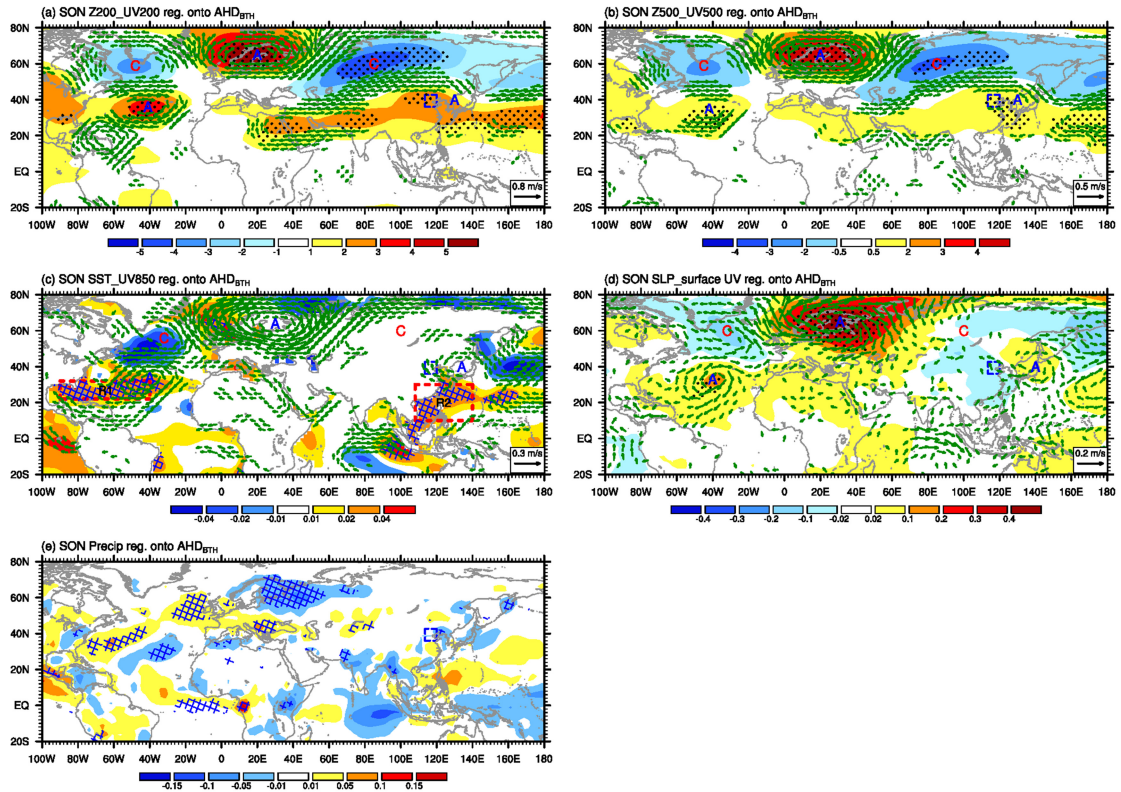
837

838

839

840

841



842

843 **Figure 5.** Regressed anomalies of autumnal (a) 200-hPa geopotential height (Z200; shaded; gpm) and 200-hPa winds (UV200; vectors;  $\text{m s}^{-1}$ ), (b) Z500 (shaded; gpm) and 500-hPa winds (UV500; vectors;  $\text{m s}^{-1}$ ), (c) SST (shaded;  $^{\circ}\text{C}$ ) and UV850 (vectors;  $\text{m s}^{-1}$ ), (d) SLP (shaded; hPa) and surface winds (vectors;  $\text{m s}^{-1}$ ), and (e) precipitation (shaded;  $\text{mm day}^{-1}$ ), with respect to the interannual component of the  $\text{AHD}_{\text{BTH}}$ . Regression coefficients that are significant at the 95% (90%) confidence level are stippled (cross hatched). In panels (a) and (b), only the wind vectors with statistical significance above the 90% confidence level are shown. In panel (c), the two red dashed rectangles, labelled R1 and R2, are the key regions where SSTAs are significantly correlated with the interannual component of the  $\text{AHD}_{\text{BTH}}$ ; vectors with scales less than  $0.05 \text{ m s}^{-1}$  are omitted. In panel (d), vectors with scales less than  $0.03 \text{ m s}^{-1}$  are omitted. The blue dashed box delineates the research domain of the BTH region. The letters A and C represent the centers of anticyclonic and cyclonic anomalies, respectively.

852

853

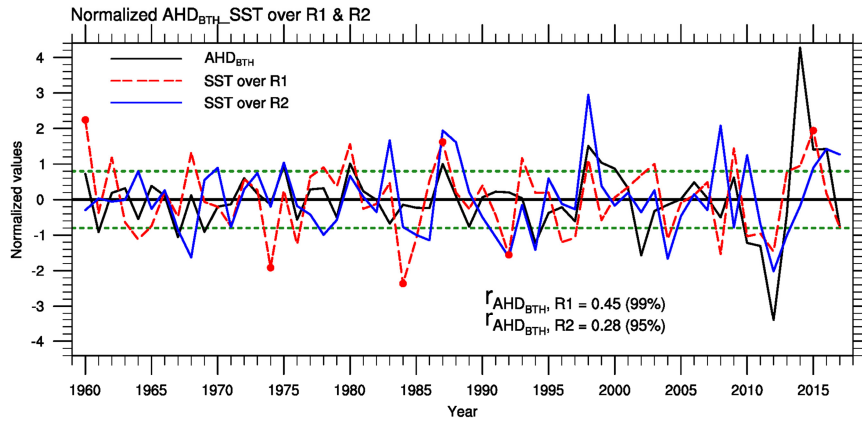
854

855

856

857

858



859

860 **Figure 6.** Time series of the normalized interannual component of the AHD<sub>BTH</sub> (black line), along with the simultaneous SST over R1  
 861 (red line) and R2 (blue line) for the period 1960–2017. The horizontal dashed lines denote 0.8 of the standard deviation. The numerals  
 862 labelled at the bottom represent the correlation coefficients (*r*) between the AHD<sub>BTH</sub> and simultaneous SST over R1 and R2, separately.  
 863 The upper and lower dots in the red line indicate the three highest and lowest years of SST over R1, respectively.

864

865

866

867

868

869

870

871

872

873

874

875

876

877

878

879

880

881

882

883

884

885

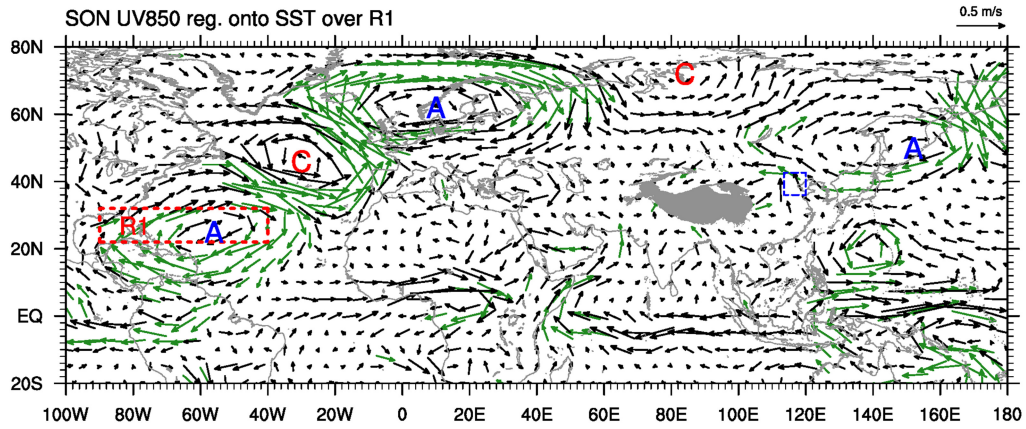
886

887

888

889

890



891

892 **Figure 7.** Regressed anomalies of autumnal UV850 (vectors;  $\text{m s}^{-1}$ ) with respect to the simultaneous interannual component of the SST  
 893 over R1. Green arrows represent the wind vectors with statistical significance above the 90% confidence level. The red dashed rectangle  
 894 labelled R1 is the key region where SSTAs are significantly correlated with the interannual component of the  $\text{AHD}_{\text{BTH}}$ . The blue dashed  
 895 box delineates the research domain of the BTH region. The gray shaded area denotes the Tibetan Plateau. The letters A and C represent  
 896 the centers of anticyclonic and cyclonic anomalies, respectively.

897

898

899

900

901

902

903

904

905

906

907

908

909

910

911

912

913

914

915

916

917

918

919

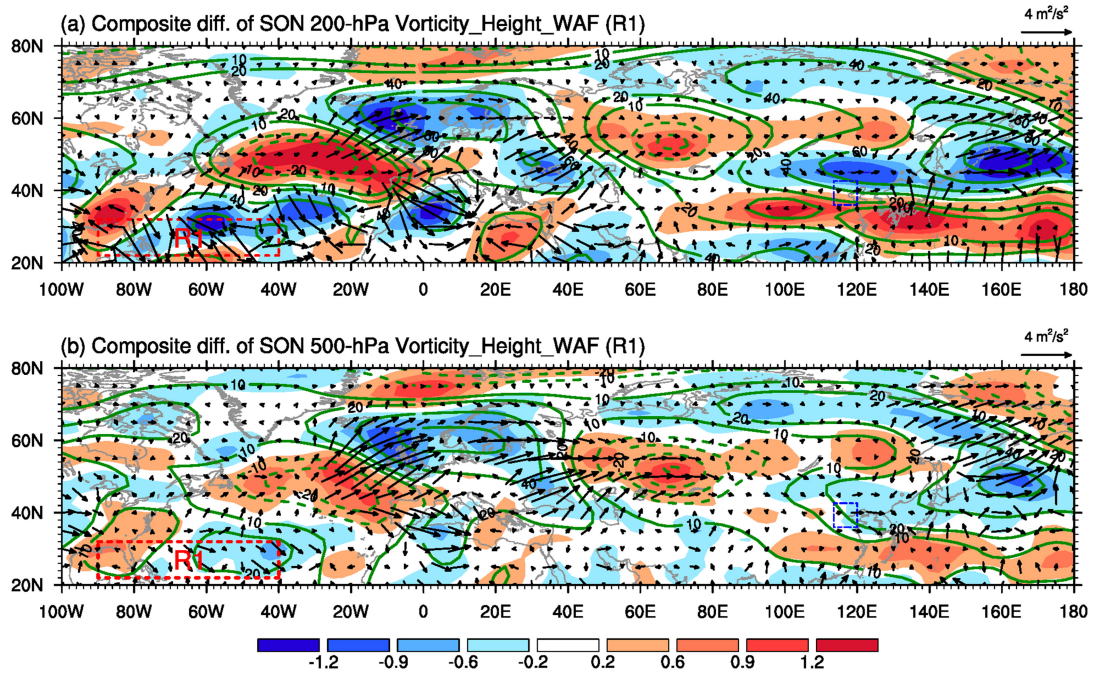
920

921

922

923

924



925

926 **Figure 8.** The autumnal composite differences of (a) 200-hPa and (b) 500-hPa WAF (vectors;  $m^2 s^{-2}$ ), geopotential height (contours;  $gpm$ ), and relative vorticity (shaded;  $10^{-5} s^{-1}$ ) between the three highest and three lowest years of simultaneous SST over R1 (highest minus lowest), as shown in Fig. 6. The red dashed rectangle labelled R1 is the key region where SSTAs are significantly correlated with the interannual component of the  $AHD_{BTH}$ . The blue dashed box delineates the research domain of the BTH region.

930

931

932

933

934

935

936

937

938

939

940

941

942

943

944

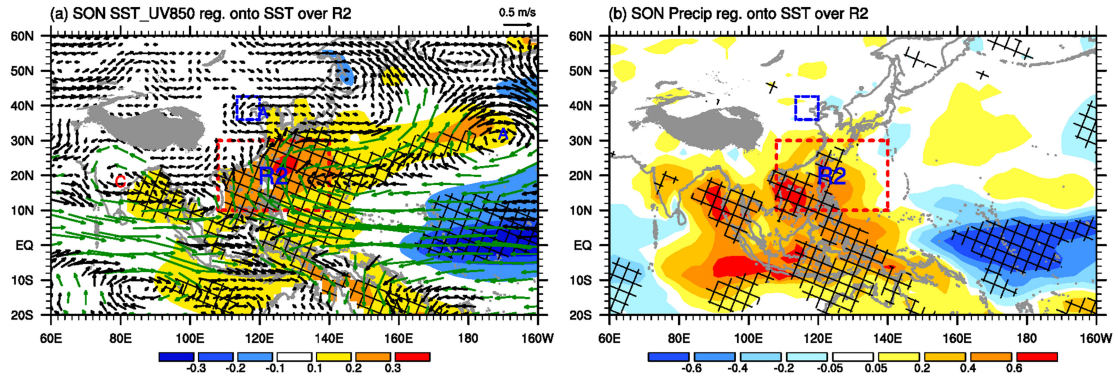
945

946

947

948

949



950

951 **Figure 9.** Regressed anomalies of autumnal (a) UV850 (vectors;  $\text{m s}^{-1}$ ) and SST (shaded;  $^{\circ}\text{C}$ ), and (b) precipitation (shaded;  $\text{mm day}^{-1}$ )  
 952 with respect to the simultaneous interannual component of the SST over R2. In panel (a), green arrows represent the wind vectors with  
 953 statistical significance above the 99% confidence level, and vectors with scales less than  $0.05 \text{ m s}^{-1}$  are omitted. Regression coefficients  
 954 that are significant at the 99% confidence level are cross hatched. The dashed red rectangle labelled R2 is the key region where SSTAs are  
 955 significantly correlated with the interannual component of the  $\text{AHD}_{\text{BTH}}$ . The blue dashed box delineates the research domain of the BTH  
 956 region. The gray shaded area denotes the Tibetan Plateau. The letter A (C) represents the center of anticyclonic (cyclonic) anomaly.

957

958

959

960

961

962

963

964

965

966

967

968

969

970

971

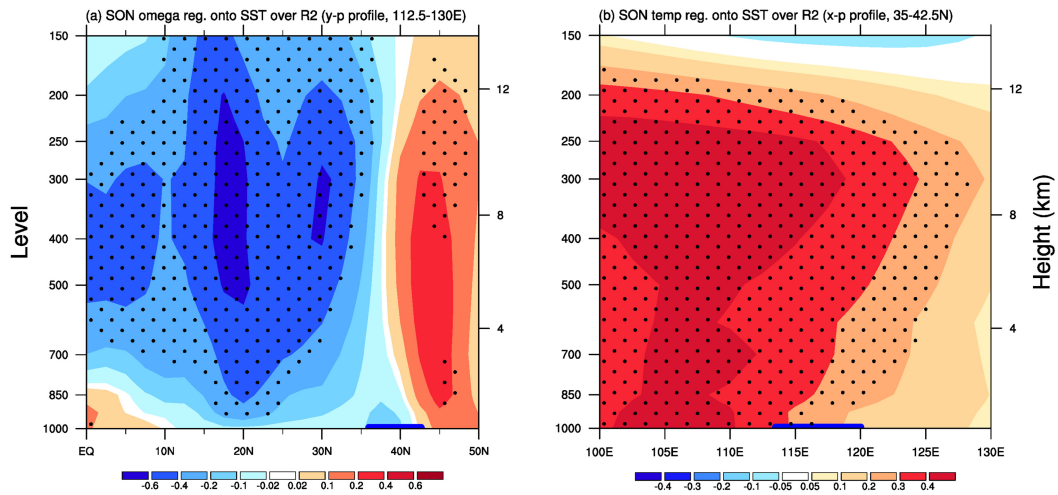
972

973

974

975

976



977

978 **Figure 10.** (a) Latitude–vertical section (112.5°–130°E) of the autumnal omega (shaded;  $10^{-2} \text{ Pa s}^{-1}$ ) and (b) longitude–vertical section  
 979 (35°–42.5°N) of the autumnal air temperature (shaded; °C) anomalies regressed onto the simultaneous interannual component of the SST  
 980 over R2. Regression coefficients that are significant at the 90% confidence level are stippled. The thick blue horizontal bars superimposed  
 981 onto the abscissa of panels (a) and (b) indicate the latitudes and longitudes of the BTH region, respectively.

982

983

984

985

986

987

988

989

990

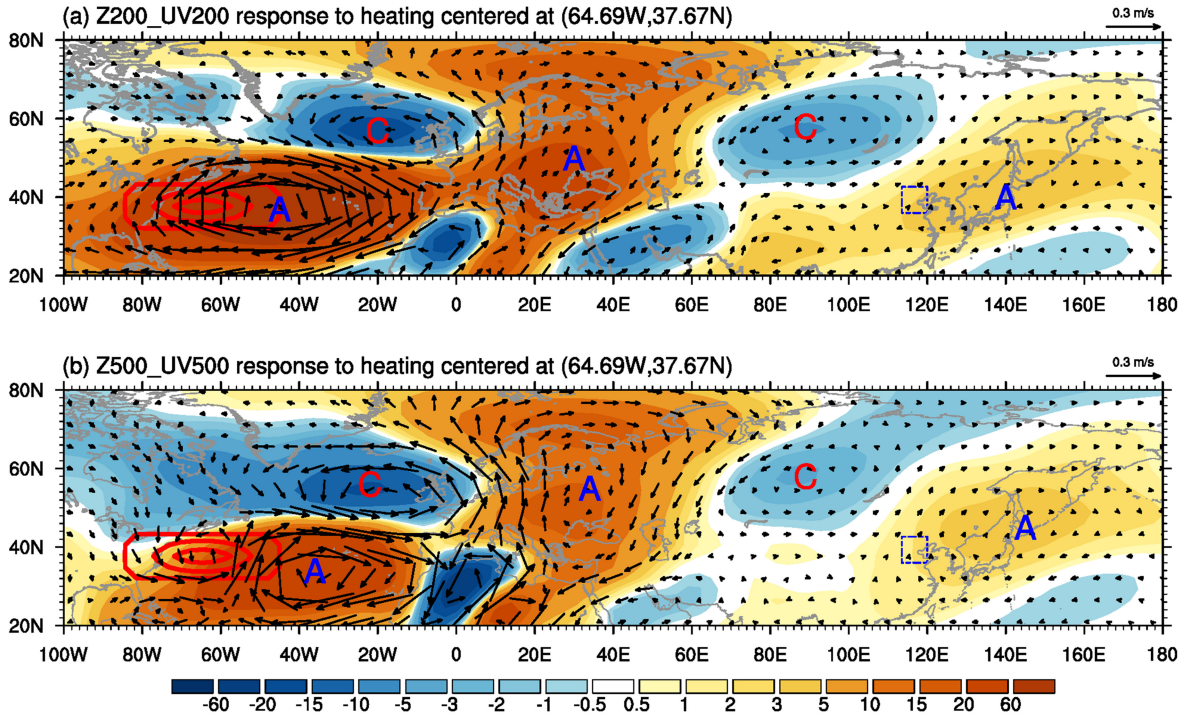
991

992

993

994





995

996 **Figure 11.** The response of anomalous (a) Z200 (shaded; 10 gpm) and UV200 (vectors;  $m s^{-1}$ ), and (b) Z500 (shaded; 10 gpm) and  
 997 UV500 (vectors;  $m s^{-1}$ ) in H\_NAS. The red contours indicate the imposed idealized heating. The blue dashed box delineates the research  
 998 domain of the BTH region. The letters A and C represent the centers of anticyclonic and cyclonic anomalies, respectively.

999

1000

1001

1002

1003

1004

1005

1006

1007

1008

1009

1010

1011

1012

1013

1014

1015

1016

1017

1018

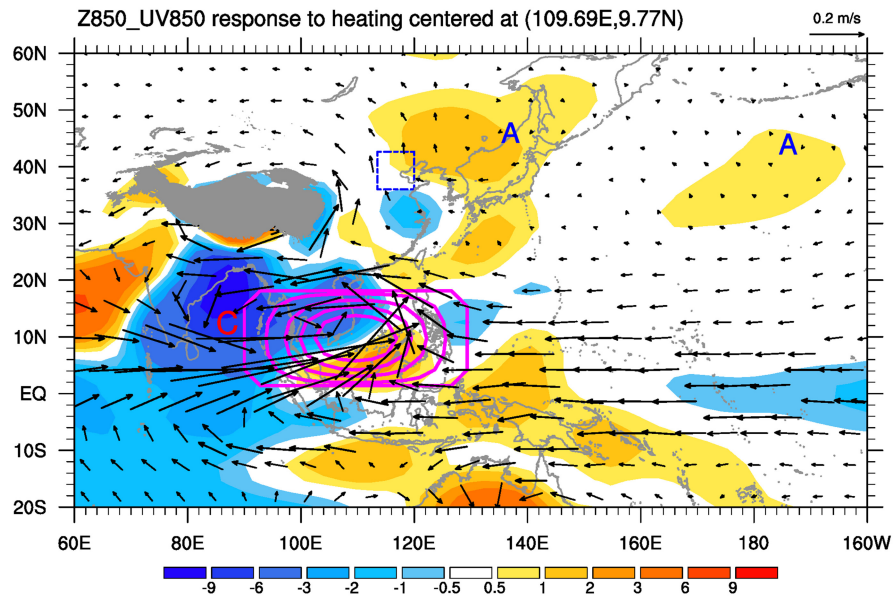
1019

1020

1021

1022

1023



1024

1025 **Figure 12.** The response of Z850 (shaded; 10 gpm) and UV850 (vectors;  $m s^{-1}$ ) in H\_WNP. The magenta contours indicate the imposed  
1026 idealized heating. The blue dashed box delineates the research domain of the BTH region. The gray shaded area denotes the Tibetan  
1027 Plateau. The letter A (C) represents the center of anticyclonic (cyclonic) anomaly.

1028

1029

1030

1031

1032

1033

1034

1035

1036

1037

1038

1039

1040

1041

1042

1043

1044

1045

1046

1047

1048

1049

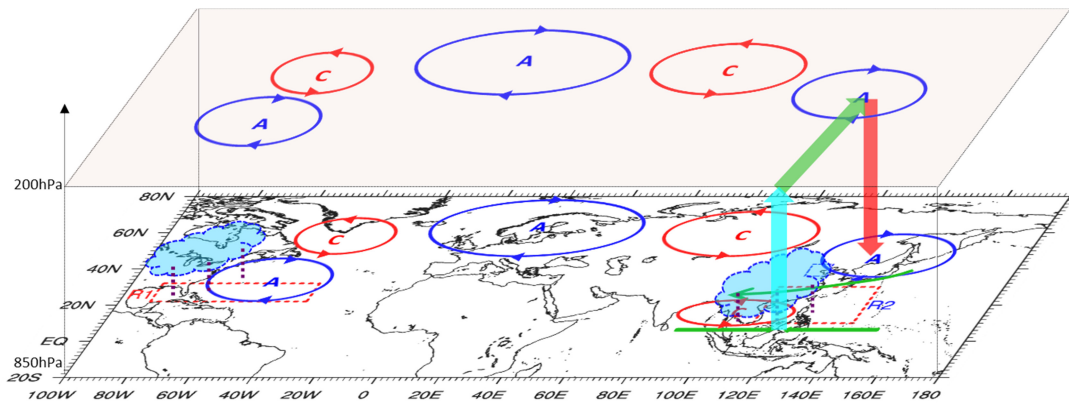
1050

1051

1052

1053

1054



1055

1056 **Figure 13.** Schematic diagram encapsulating the SSTA-induced (warming in R1 and R2) physical mechanisms and pathways connected to above-normal  $AHD_{BTH}$  years on the interannual timescale. Anomalous quasi-barotropic anticyclones (A) and cyclones (C) are indicated by blue and red elliptical cycles with arrows separately, denoting large-scale Rossby wave train triggered by the heating to the north of R1. Green arrows depict the key horizontal low-level (850-hPa) airflows. The red, azure and green arrows together exhibit the vertical overturning circulation tied to the SST warming in R2. The left-hand (right-hand) side of the cloud-resembled pattern with violet short dashed lines presents the significant anomalous precipitation induced by SSTAs over R1 (R2). The blue dashed box delineates the research domain of the BTH region.

1063

1064

1065

1066

1067

1068

1069

1070

1071

1072

1073

1074

1075

1076

1077

1078

1079

1080

1081

1082

1083

1084

1085

1086

1087

1088

1089